AKADEMIA GÓRNICZO-HUTNICZA IM. STANISŁAWA STASZICA W KRAKOWIE
WYDZIAŁ ENERGETYKI I PALIW

KATEDRA ZRÓWNOWAŻONEGO ROZWOJU ENERGETYCZNEGO

Praca dyplomowa

magisterska

Investigation of Li-ion battery cell thermal conditioning and its effect on aging and performance in lab and automotive environment

Badania wpływu kondycjonowania termicznego ogniw litowo-jonowych na starzenie się i wydajność w środowisku laboratoryjnym i samochodowym

Autor: *Yichun Zhang*
Kierunek studiów: *Energetyka Odnawialna i Zarządzanie Energią*
Opiekun pracy: *dr hab. inż. Kun Zheng, prof. AGH*

Kraków, 2023

Abstract

The rise of electric vehicles (EVs) is a key solution to reduce the transport sector's environmental impact, driven by advances in lithium-ion battery (LiB) technology which has increased energy density and reduced costs. However, temperature significantly affects the performance of the battery, necessitating effective cooling strategies and accurate modeling approaches to ensure their longevity and efficiency in real-world conditions. This thesis develops an electro-thermal 3D model through COMSOL Multiphysics 6.0, which integrates the second-order resistance and capacitance (2RC) equivalent circuit models (ECM) for heat generation with the finite element analysis (FEA) heat transfer model based on the cell's geometry. The simulation results present the internal temperature distribution and voltage response of the cell based on the applied load cycle, supporting the optimization of cooling strategies for the cell.

Streszczenie

Wzrost popularności pojazdów elektrycznych (EVs) jest kluczowym rozwiązaniem mającym na celu ograniczenie wpływu sektora transportu na środowisko, napędzanym przez postępy w technologii baterii litowo-jonowych (LiB), które zwiększyły gęstość energii i obniżyły koszty. Jednak temperatura znacząco wpływa na wydajność baterii, co wymaga skutecznych strategii chłodzenia i dokładnych metod modelowania, aby zapewnić ich długowieczność i efektywność w rzeczywistych warunkach. Niniejsza praca rozwija elektro-termiczny model 3D przy użyciu COMSOL Multiphysics 6.0, który integruje modele drugiego rzędu oporu i pojemności (2RC) równoważne z modelami obwodów (ECM) dla generacji ciepła z modelem transferu ciepła opartym na metodzie elementów skończonych (FEA) opartym na geometrii ogniwa. Wyniki symulacji przedstawiają wewnętrzny rozkład temperatury i odpowiedź napięciową ogniwa w oparciu o zastosowany cykl obciążenia, wspierając optymalizację strategii chłodzenia dla ogniwa.

Nomenclature and abbreviations

AC	Alternating Current
BMS	Battery Management System
BTMS	Battery Thermal Management System
DEC	Diethyl Carbonate
DMC	Dimethyl Carbonate
EC	Ethylene Carbonate
ECM	Equivalent Circuit Model
EIS	Electrochemical Impedance Spectroscopy
Evs	Electric Vehicles
FEA	Finite Element Analysis
FEC	Fluoroethylene Carbonate
FEM	Finite Element Model
I	Current
IEA	International Energy Agency
LiB	Lithium-Ion Battery
Li-NCA	Lithium Nickel Cobalt Aluminum Oxides
LiPF6	Lithium Hexafluorophosphate
LP	Lumped-Parameter
LTO	Lithium Titanate Oxide
LUT	Look-Up Table
NE	Negative Electrode
OCV	Open Circuit Voltage
P2D	Pseudo Two-Dimensional
PE	Positive Electrode
R2	The Second Parameterization Resistance
SOC	State-Of-Charge
T	Temperature
2RC	The Second-Order Resistance And Capacitance
3D	Three-Dimension

Table of Contents

1. Introduction

1.1. Li-ion battery

Electrification of vehicles is regarded as one of the most essential solutions for reducing the environmental impact of transport sector, supported by governments, conducted by manufacturers, and adopted by customers. The days of the fossil-fueled vehicle are numbered and tailpipe emissions are anticipated to reduce. Therefore, there are more and more electric vehicles (EVs) hit the roads in recent years worldwide. Data presented by the International Energy Agency (IEA) shows EV purchases have been growing at least 30% year-by-year since 2016 [1].

In the last two decades, the barrier to EV passive production could be mainly attributed to its short drive range and expensive manufacturing costs. With significant advancements in battery technologies catalyzed by pioneering contributions such as Sony's launch of the first commercial lithium-ion batteries (LiBs) [2], a new era has emerged for energy storage systems. This evolution, epitomized by the progressive development of LiBs, boasts commendable attributes including enhanced energy density, cost-effectiveness, and extended cycle life. These improvements enable LiBs to facilitate extensive driving range and rapid acceleration, thereby driving the expansion of their applications across diverse domains.

LiBs, being the costliest component of EVs, have garnered significant attention, particularly concerning the optimization of their utilization. Anticipations revolve around enhancing their performance and extending their lifecycle. Considering these two factors are usually evaluated on different integration levels, from the cell level, the smallest unit, connected to the module level, linked with electric wires to the pack level. Considering the elevated costs and intricate mechanism associated with conducting tests at the battery system level, opting to commence with a primary focus on the cell level becomes both a pragmatic and sensible approach. However, it's important to note that such cell level testing

introduces challenges associated with constructing a truly representative test environment.

In most cases, the performance of the LiB cell is largely influenced by temperature. It is researched that its optimal temperature range is 15~35℃ [3]. However, in typical scenarios, the practical working temperature range extends from -20°C to 60°C, substantially exceeding the ideal comfort zone. This discrepancy has negative impact on the performance, lifespan, and safety of LiBs, which can be discussed and analyzed from the effects of high temperature and low temperature. During the cycling process, LiBs generate considerable heat that influences the operational temperature. To maintain a stable working temperature range for LiBs, various cooling strategies have been implemented. Furthermore, gaining a better understanding of the linkage between aging and thermal conditioning could help finding more optimized cooling stategies to prolong LiB life and improve performance.

LiBs have been a mature energy storage technology in recent years, and a vast amount of research has paid close attention to how to build a more idealized automotive environment. However, there are still unresolved issues. Even though a lot of thermal and electrochemical simulations were performed to analyze the implications of the thermal environment and cooling strategy, in many cases, the simulation models and assessments based on cell level tests are with limited understanding of how the differences in thermal environment in cell level test, which might impact the results in terms of LiBs performance and life. Thus, an ambition is that coupled with lab experiments on LiB cells in different thermal conditioning, a model for LiB cell is expected to get developed, which could help with a deeper comprehension of a more suitable test setup to replicate a realistic vehicle-like environment and develop an effective temperature-controlling method to keep the operating temperature within a specific range.

1.2. Working principles

LiB cell operates through the redox reaction and the basic working principle is based on the transfer of ions of lithium. Every component of LiB cell is effective

for its operation. During discharging, the lithium ions leave negative electrode, enter electrolyte, and travel through the separator to the positive electrode, creating the internal circuit. At the same time, electrons from negative electrode are also released to keep the electric equilibrium, and move to positive electrode through the external circuit. During charging, the process and transfer are reversed. What needs to note is that electrons are powered by the load to move from positive to the negative electrode.

Taking lithium nickel cobalt aluminum oxides (Li-NCA) cell, one of the most potential next generation of LiB technologies to enter and take over the market in the following ten years by IEA [1], as an example, the reactions and the transfer of ions and electrons during charge and discharge are illustrated in **Figure 1.1** and equation (1) - (3).

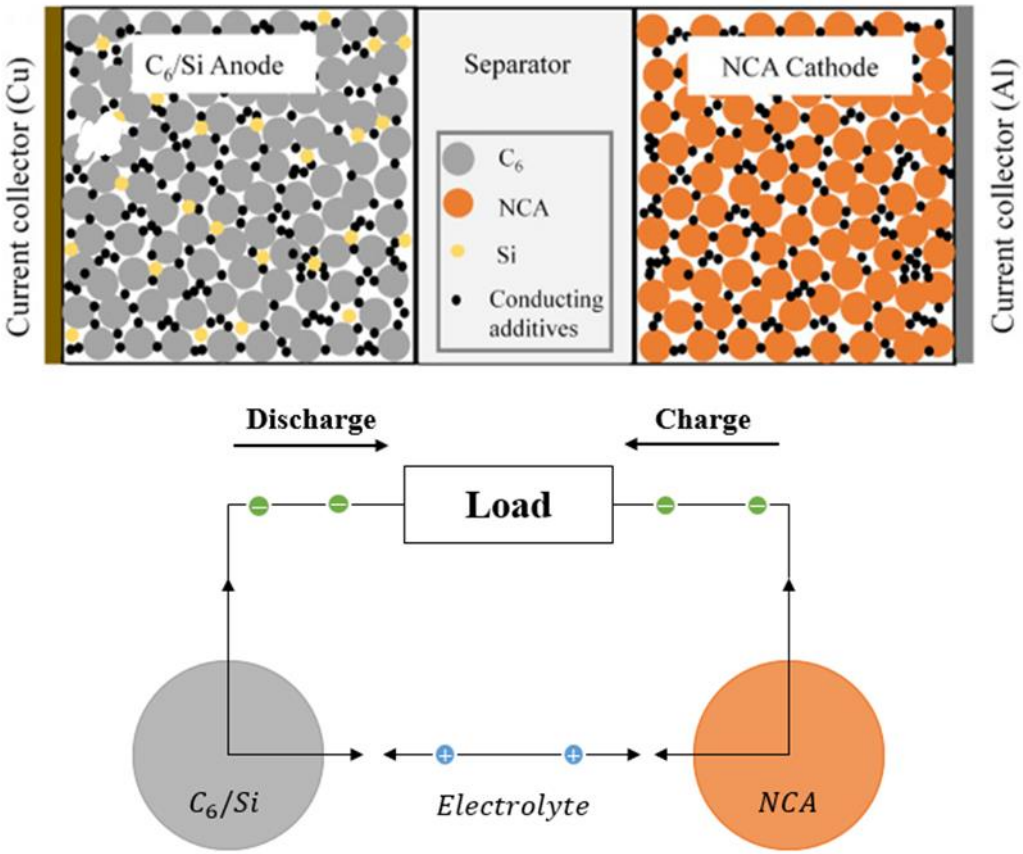

Figure 1.1 An example of Li-NCA cell chemistry. The anode active materials are C6 and Si particles, and the active material in the cathode is NCA particles [4,5].

C_6/Si: $$C_6 + y\mathrm{Li}^+ + ye^- \underset{\text{discharge}}{\overset{\text{charge}}{\rightleftharpoons}} \mathrm{Li}_y C_6, 0 \le y \le 1 \quad (1)$$

C_6/Si: $$4\mathrm{Si} + z\mathrm{Li}^+ + ze^- \underset{\text{discharge}}{\overset{\text{charge}}{\rightleftharpoons}} \mathrm{Li}_z\mathrm{Si}_4, 0 \le z \le 15 \quad (2)$$

NCA: $$\mathrm{LiNi_{0.85}Co_{0.1}Al_{0.05}O_2} \underset{\text{discharge}}{\overset{\text{charge}}{\rightleftharpoons}} \mathrm{Li_{1-m}Ni_{0.85}Co_{0.1}Al_{0.05}O_2} + m\mathrm{Li}^+ + me^- \quad (3)$$

1.3. Cell design

The main essential components of LiBs cell consist of positive electrode (PE), negative electrode (NE), electrolyte, and separator, which work as different roles during the LiBs cell operation. In general, the aluminum and copper foils perform as current collectors, and the negative electrode materials are coated on the former, while the positive electrode materials are coated on the latter. Both electrodes and the separator are soaked in electrolyte. All these components will be described in more detail in following sections.

1.3.1. Negative electrode

The material of the negative electrode shows significant effects on the performance of the LiBs cell since the inherent electric potentials vary with electrode materials. In the design of the LiB cell, certain important parameters are prioritized, such as rate capacity, coulombic efficiency and power density [6]. The carbon-based compounds, especially graphite, are most-commonly used materials for commercial negative electrode considering its abundance, high electrical conductivity, and low prices [7]. However, with slow diffusion and sustained deposition of lithium ions, it results in the problem of dendrites to graphite electrode. Silicon composite electrodes works as the alternatives to increase the capacity of electrode [6]. For greater safety, longer cycle life, and higher rate capacity, alloys and transition metal oxides, for example, lithium titanate oxide (LTO), are also great options for negative electrode. All these four categories for negative electrode are with promising features, but also with limitations

correspondingly, which requiring to select suitable material to reach the full performance of LiBs cell and fulfill target demands [6].

1.3.2. Positive electrode

The voltage and capacity are different between negative and positive electrodes. The ideal design for the LiBs cell is to reach the high capacity and high voltage simultaneously with desirable choices of electrode materials, according to which, **Figure 1.2** contributes to make a balanced cell. Lithium transition metal oxides, for example $LiCoO_2$ (LCO), attracted research attention for positive electrode materials due to their high structural stability and mature production process. However, the extraction of cobalt presents notable ethical concerns, particularly in the Democratic Republic of the Congo where the largest known reserves are localized [8], together with its high cost and safety issues hindered itself applied to large batteries system [9,10]. Aiming this, the group of transition metal phosphates containing lithium, such as $LiFePO_4$ (LFP), was regarded as a promising alternative due to its lower cost, better safety, and higher abundance. Besides, other lithium transition metal oxides with layered structure, such as $LiNi_{1-x-y}Co_xAl_yO_2$ (NCA) and $Li_{1+a}(Ni_xMn_yCo_z)_{1-a}O_2$ (NMC) distinguish themselves with stable structure, superior cyclability, and good electrochemical performance, exhibiting both remarkable potential and capacity as well as high energy density, which also suppresses the capacity fading [9,11].

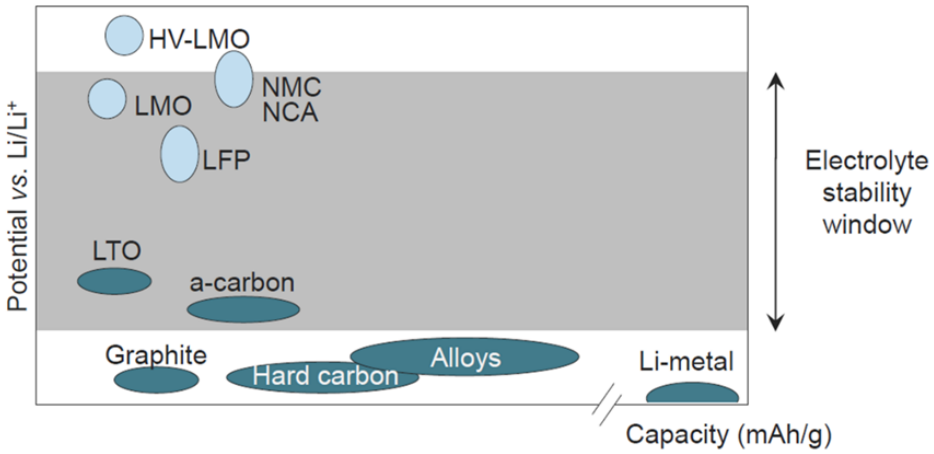

Figure 1.2 Approximate electrode potential vs capacity for various electrode materials [7]. The grey area indicates electrolyte stability window.

1.3.3. Electrolyte

Considering the electrolyte mediates the ion transfer between the positive and negative electrodes, in another words, it defines the rate of the energy released and limits the mass flow of the LiB cell [7], making the electrolyte important to obtain excellent performance of LiB. Thus, electrolyte is expected to be characterized with thermal and electrochemical stability, high ionic conductivity, and low viscosity over a wide temperature [12]. Besides from function side, the safety aspect is crucial, requiring the tolerance of electric, mechanical, and thermal abuse as well as low flammability. Thus, to fulfill these requirements possibly, the most commonly used liquid electrolytes consist of a mixture of a lithium salt in organic solvents in commercial LiBs. More specifically, the most widely applied one is composed of a solution with lithium hexafluorophosphate (LiPF6) in mixtures of carbonates, such as ethylene carbonate (EC), dimethyl carbonate (DMC) and diethyl carbonate (DEC) being the most used ones [13,14].

1.3.4. Separator

The separator in a battery, is a critical component, placed between positive electrode and negative electrode. Its primary function is to prevent direct physical and electrical contact between the electrodes, thereby avoiding a short-circuit within the battery cell. While the separator itself does not participate in the electrochemical reactions that occur during the charging and discharging of the battery, it plays a crucial role in influencing the overall performance and safety of the LiB cell. One important aspect is that the separator serves as a reservoir for the electrolyte, allowing the transport of ions between the electrodes. To fulfill its function effectively, the separator needs to strike a balance between high electric resistance and sufficient porosity [15]. High electric resistance helps to minimize the flow of electrons between the electrodes, preventing internal short-circuits. On the other hand, sufficient porosity allows the electrolyte and ions to move freely within the battery, facilitating efficient ion transport. Achieving this balance is crucial for maintaining optimal battery performance. There are different types of separators used in LiB technology. Single-layer and multilayer separators are greatly mature and common technologies, composting from polyolefins to blends

and composites of fluorinated polymers. Besides, ceramics addition and surface modification are also applied to obtained desired properties, such as thermal stability, mechanical strength, and electrolyte retention [16].

1.3.5. Mechanical design of LiBs

For every LiB cell, there are two poles, known as tabs, which are often placed with a gap in between or on opposite sides of the cell, enabling electrical connection between current collectors and external circuit. Usually, the cell is assembled by stacking or rolling all its layers together into a jelly roll, which is then placed inside the cell can. The can is sealed, leaving only a small hole. Subsequently, the electrolyte is injected through the hole into the cell before sealing it completely to prevent any leakage [17]. To pack all their components, three types of structure are adopted in current commercial cells: cylindrical, prismatic and pouch (**Figure 1.3**). Cylindrical cells are widely used over the year. Their common formats are 18650 as well as 21700, and the new standard is 46XX , which different versions and models of Tesla vehicles [18]. Due to a higher tension from wound electrodes, the energy density of 18650 cell reaches around 600 Wh/L, a fifth higher than the rest [19]. To fulfill higher degrees of design freedom, the prismatic and pouch cells stand out. The prismatic cell is suitable to integrate, easy to cool, and robust to get packed assembly, making some EV manufacturers in favor with which despite the relatively expensive manufacturing costs. The pouch cell eliminates the metal enclosure and enables highly efficient space usage of 90% packaging efficiency [20]. Therefore, prismatic and pouch cells make them easily customized for the final product, compensating for the sacrifice of slight energy density compared to the cylindrical cell [19,20].

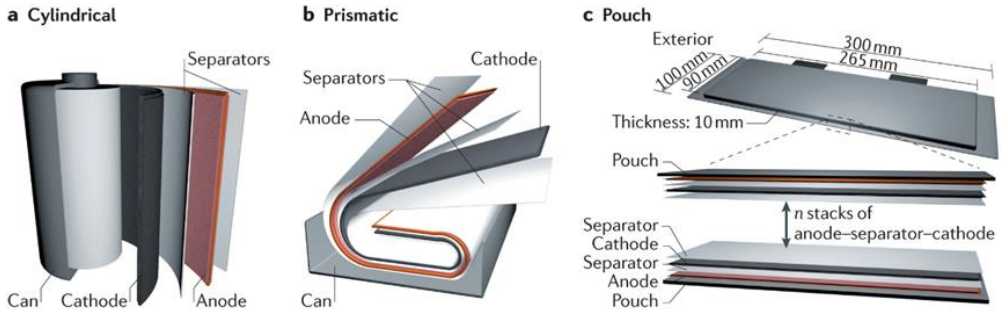

Figure 1.3 Three representative commercial cell structures [19].

1.4. Typical vehicle battery

In practical cases, high energy and power are needed for vehicle applications. Thus, automotive manufactures use several battery cells connected in series and parallel for suitable voltage and energy levels. As shown in **Figure 1.4**, the battery pack in the Tesla Model S comprises 16 modules, with a total of 7,104 cylindrical 18650 Li-NCA cells, whose configuration allows to achieve the energy of up to 85 kWh. In every module, there are 6 series of 74 cells connected in parallel [5,18,21]. Besides, other typical vehicles' battery is listed in **Table 1.1**.

Figure 1.4 Battery of Tesla Model S: module level (a) and pack level (b) [18,21].

Table 1.1 Summary of different LiB for passenger cars [20]

	Cell		Energy (kWh)	Cooling strategy
	Mechanical design	**Chemistry (NE/PE)**		
Nissan Leaf (2015)	Pouch	Graphite /LMO-NCA	30	Liquid cooling
Renault Zoe (2017)	Pouch	Graphite /NMC	41	Air cooling
Tesla Model S (2012)	Cylindrical	Graphite /NCA	85	Liquid cooling
Volvo XC60 (2017)	Prismatic	NMC	10.4	Liquid cooling
BMW I3 (2017)	Prismatic	Graphite /LMO-NCA-NMC	33	Liquid cooling

2. Aim and scope

This thesis focuses on the LiB cell, especially on the Ni-rich Li-ion prismatic cell. It is aimed to develop a model to support optimization of both cooling strategy and test environment. It was witnessed by 2019 from IEA that Europe saw a 50% increase in EV sales, leading to an increase in its market share [1], which suggests a huge potential for LiBs, and bring both opportunities and challenges to improve the improve the cell performance and prolong the lifetime of LiB cell.

There are multiple expectations for the characteristics of LiB cell, including the propulsion power, driving range, charging speed rate, durability, and safety. When fulfilling these requirements, LiB cell's performance in these aspects are highly dependent on temperature. Different thermal conditioning leads to different electrochemical behaviors. Regarding this, the research questions are described as following:

1) At the cell level, what is the effect on cell performance and life from thermal conditioning?

2) What are the common cooling strategies for LiBs? What is the thermal performance of LiBs when applying different cooling strategies?

3) How to bring the cell testing environment/setup close to thermal conditioning in an automotive environment?

4) How to improve the performance of LiB cell and lessen its ageing in the automotive environment?

The first two questions were answered in the literature review, and the third question was the key issue discussed in the thesis by: a) developing an electric-thermal three-dimension (3D) model of the Ni-rich Li-ion prismatic cell, b) contributing to support the optimization of cooling strategies and helping to design a realistic vehicle-like test environment. The answer to last question was summarized in the analysis of the simulation and lab work, as well as contributing to the conclusion of the thesis.

3. Literature review

3.1. Effects from different thermal conditioning

3.1.1. High temperature

Recently, the NCA cathode was used in Tesla Model S due to its high power density and capability of driving around 400 km per single charge [18]. However, when cycling over 100% DOD for 140 cycles at 25℃ and 60℃ relatively, the capacity fade of NCA/C_6 cells showed a huge difference. The high-temperature cell lost 65% of its initial capacity, which was 20 times more than the room-temperature one [22]. It suggested that the Li-NCA cell met problems of poor thermal characteristics and accelerated capacity deterioration at elevated operation temperatures [23,24]. The reversible capacity was achieved by the high relative content of Ni with the sacrifice of thermal stability, leading to the formation of NiO-like structure layer, contributing to the increase in impedance and degradation of the NCA cathode, accelerating the cell ageing leading to thermal runaway [25].

It is reported that, at rising temperatures, significantly above 55 ℃, the performance of the cell degrades greatly compared to those operates in normal temperature range, indicating the capacity fade and the power loss. **Figure 3.1** (a) shows that even the elevated temperature could increase cell's performance through increasing its capacity temporarily in a period, but the maximum charge storage capacity fades irreversibly with the temperature, which is mainly attribute to the lithium loss and active reduction inside the cell, suggesting side reactions between the cathode and electrolyte [5,26], which can be improved by coatings and surface modification [27]. **Figure 3.1** (b) shows the increasing cell internal resistance with increasing cycling temperatures, leading to the loss of the power. According to Leng's analysis regarding the effect of high temperature towards LiB cell's performance, the elevated temperature accelerates all components' degradation of LiB cell, not only affecting the maximum charge storage capacity and internal resistance, but also the coulombic efficiency and charge transfer rate constant of electrode [28]. To improve cell performance and prolong its lifespan,

it is of great significance to conduct the thermal management to control the temperature.

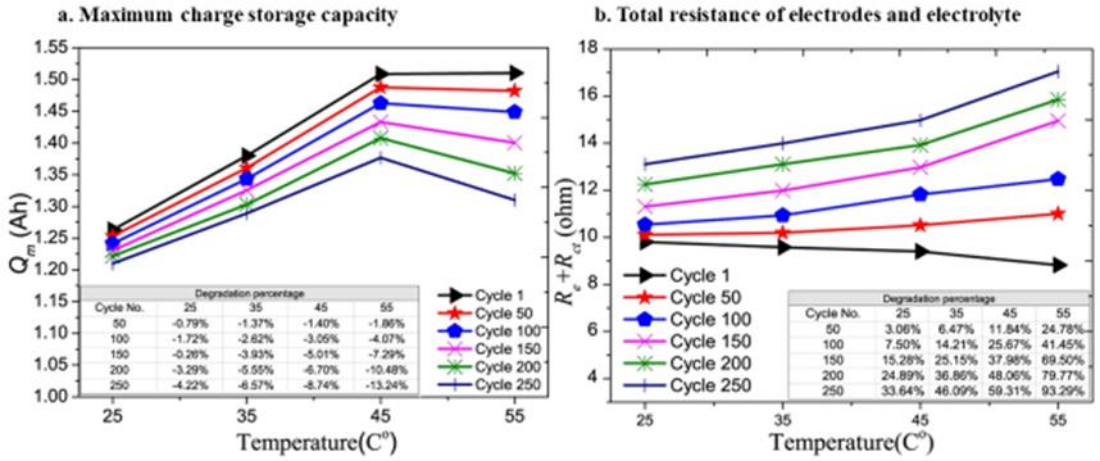

Figure 3.1 The maximum charge storage capacity corresponds to temperatures and cycle numbers (a); The total resistance of electrodes and electrolyte corresponds to temperatures and cycle numbers (b) [28].

Thermal runaway is another inevitable issue and widely researched phenomenon when it comes to high temperature effects, which might lead to severe consequence and present serious safety problems. Thermal runaway in LiB cell encompasses a cascading sequence of interconnected processes and reactions, where heat generation intensifies correspondingly with rising temperatures, and it occurs when all the exothermic reactions in the cell triggers sequentially by the heat released, finally leading to fire with the generation of large amount of deleterious gas and explosion in more severe cases [29]. During this process, the temperature can reach extremely high to 870 ℃ [5], and the reactions persist unabated without external intervention, ultimately causing the cell's destruction through heat-induced mechanisms [29]. Thermal runaway involves a series of complex reactions, including decomposition of the solid-electrolyte interface (SEI), the chemical reactions encompassing the electrolyte and electrode with binder, and the decomposition of the electrolyte, etc. [29–31]. It is proposed that thermal runaway can start when the cell temperature rises above 80 ℃, and the process and stages are shown in **Figure 3.2** and **Figure 3.3**.

Figure 3.2 Process of thermal runaway in reality [17].

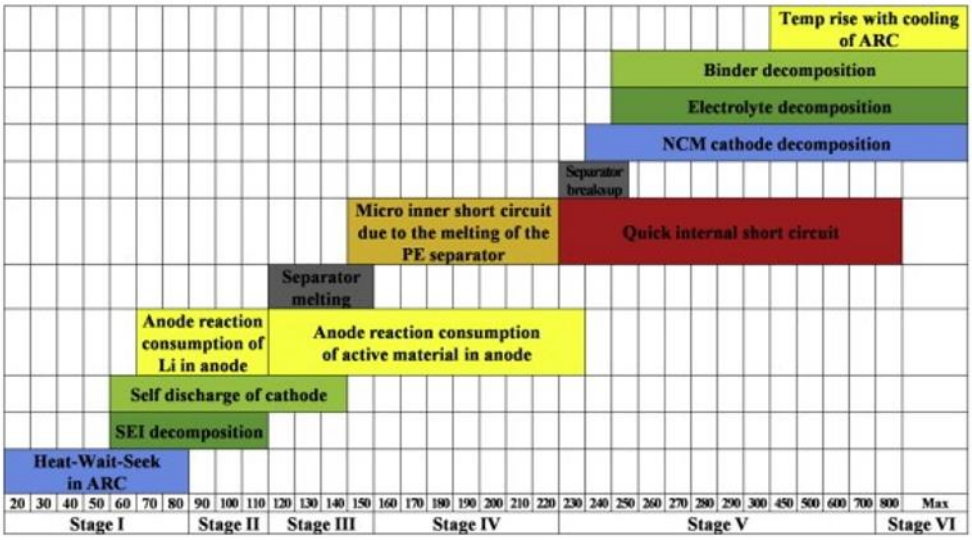

Figure 3.3 Stages of thermal runaway at different temperature ranges [31].

3.1.2. Low temperature

At low temperatures, the viscosity of electrolytes would rise with the dropping temperature, resulting in a sharp decrease in ionic conductivity and hindering the ion transport in electrolytes, which leaded to an increase in resistance and a reduction in energy density (**Figure 3.4**) [32,33]. To solve this problem and maintain normal function at low temperatures, using additives is regarded as one of the most convenient and economical ways by the industry [34]. With no more than 5% additives (either by weight or by volume), the viscosity and freezing point of electrolytes reduce effectively. For example, additives with fluorine groups, like

Fluoroethylene carbonate (FEC), could decompose on the surface of graphite to induce a thin and compact SEI layer [35].

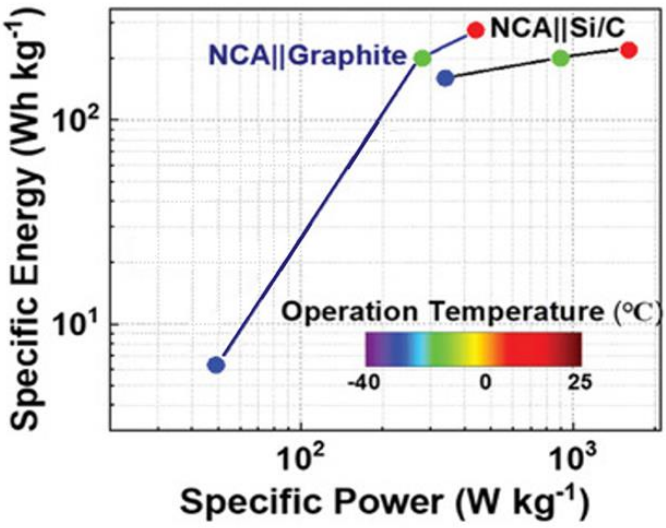

Figure 3.4 Energy/power density of typical NCA cells at 25, -20, and -30 ℃ [33].

Zhang presented that the poor performance of the Li-ion battery at low temperatures was mainly attributed to the increase in charge-transfer resistance, resulting in the slow kinetics of the electrode reactions [36]. It also led to the problem of Li^+ desolvation, confirmed as the main barrier to Li^+ transfer and the rate-controlling step at low temperatures [37]. Also, the higher charge-transfer resistance makes charging more difficult than discharging in cold conditions [38].

Lithium plating is a typical issue that needs to be solved operating at a low temperature [33,38]. The cold condition leads to a trend of anode polarization, making the potential for Li^+ intercalation into graphite almost reach lithium plating [39]. It is occurring when metallic lithium deposits on the anode surface instead of inserting itself into the anode through intercalation [40]. The produced Li dendrite is clustered on the surface of the cathode, blocking the electrode reactions and degrading the lifetime of the battery [5]. To tackle this problem, LTO can be used as an alternative to graphite, making the difference in equilibrium potential higher and contributing to the cell being much less sensitive to lithium plating. However, it will not be the perfect solution. Due to the low nominal voltage of the LTO cell, the energy density is significantly lowered [38].

To obtain the better performance of the Li-ion battery cell in cold conditions, preheating technologies, fundamentally rising the operating temperature to solve the problems, are regarded as the most effective methods [41]. Among them, the self-heating technology, especially using pulse and alternating current (AC) to generate heat through the internal impedance to preheat the cell core terminal, is with high energy efficiency and good temperature uniformity. In addition to preheating, the utilization of insulation materials, such as aerogel, can effectively maintain the temperature of the LiBs system by providing exceptional thermal insulation [42]. These materials serve to mitigate the effects of low ambient temperatures. The impact of insulation materials is also influenced by their thickness, where an optimal thickness, typically around 10 mm, results in a substantial thermal resistance [42,43].

3.1.3. Cases study of Failed BMS

As the most expensive part of the vehicles, LiBs failure can result in more severe consequences such as passengers' injury, besides the vehicles damage. The main hazards associated with batteries commonly arise from extreme temperatures, external or internal short circuits, as well as overcharging or over-discharging, which may trigger exothermic reactions within the battery [44]. The disaster would happen if the temperature of LiB reaches sufficiently high or with an available ignition source, which might ignite the flammable gases from LiB, meeting the condition of the fire (**Figure 3.5**). The cases of EV fire are presented in **Table 3.1**.

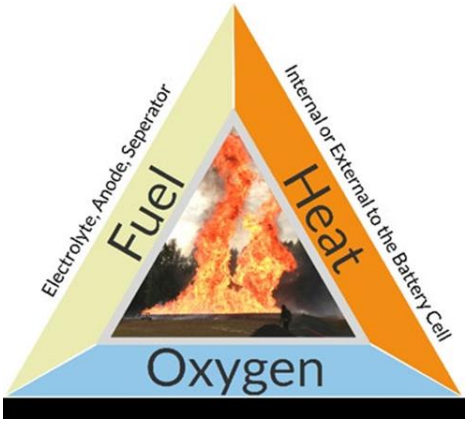

Figure 3.5 The fire triangle for LiB [44].

Table 3.1 Summary of some documented EV fire incidents [44]

Vehicle	Incident	Cause	Location	Year
Tesla Model S	Fire when plugged to Tesla supercharger station	Short circuit in electrical system of the car	Oslo, Norway	2016
Tesla Model S	Struck wall and pole, immediate fire	Battery case ruptured	Florida, USA	2018
BMW I8	Smoke from the front, parked in showroom at dealership	/	Tilburg, Netherlands	2019
Rebuilt Nissan Qashqai	Fire during charging	/	On Ferry "Pearl of Scandinavia"	2010
Chevrolet Volt	Fire 3 weeks after crash test	Leaking coolant in battery	Wisconsin, USA	2011
2 Bolloré Bluecar	Fire in parked vehicle and spread to second vehicle	Vandalism	Paris, France	2013

To improve the fire safety of LiBs, a holistic solution is proposed. In an optimal scenario, the single LiB cell would be expected to mitigate the occurrence of short circuits, which might lead to overheating and thermal runaway. As for the module level, it was designed to prevent the propagation of thermal runaway among the cells. When it comes to pack level, the safety systems capable of detecting and preventing potential fires were supposed to get equipped. Besides, the battery management system (BMS) would effectively and smartly deal with the battery issues and even be able to interact with other vehicles [44].

3.2. Cooling strategies

Implementing efficient cooling strategy and deploying battery thermal management system (BTMS) are vital to maintain the working temperature of LiB cells within a normal range and ensure their performance, safety, and longevity. To choose the appropriate cooling strategy, several factors need to be taken into consideration, including cost, complexity, weight, cooling efficiency, temperature uniformity, and parasitic power [5], which are elaborated clearly on the most commonly used cooling strategies in the following sectors.

3.2.1. Air cooling

Air cooling, the most traditional cooling method, has been extensively researched and widely used in commercial automotive applications, especially in some parallel HEVs, such as Toyota Prius, because of its distinct advantages of simplicity, lightweight and low cost [5,19]. Generally, according to if the inlet air is cooled by the external force, the air cooling BTMS are further classified as natural convection (or passive) and forced convection (or active) systems, while the heat transfer coefficient of the former is much lower than that of the latter [5]. Also, Nelson pointed the ineffectiveness of passive air-cooling method in lowering the temperature of the battery pack when reaching as high as 66℃ [45], showing the limited availability of passive air-cooling strategy for low energy density batteries. Thus, the general air-cooling system is driven by several fans or blower, helping a lot to enhance the heat transfer coefficient, and cools down cells through forced air flowing past the surfaces of cells, the efficiency of which differentiates by configurations and parameter settings [5,46].

The configurations of air-cooling system affect its cooling efficiency and thermal behavior of battery, which can be categorized as series, series-parallel mixed, and parallel, shown in **Figure 3.6**. According to Xia's research, the design of simple channel with reciprocating cooling, **Figure 3.6** (c), achieved a combination of temperature uniformity of cells and reducing the parasitic power, which refers to the energy consumed by the cooling system itself is considered wasteful concerning the overall efficiency of the cell system, only with slight

sacrifice of 0.5 ℃ final cooling results, compared to other series cooling configurations [46]. Pure parallel cooling configurations, shown in **Figure 3.6** (d) and (c), were the best choice for minimizing the temperature difference in battery module. The series-parallel mixed cooling configuration can be regarded as an optimization of series and parallel cooling configurations with great reduction in flow path, relative increase in the cross-sectional area of channel, and much improvement in temperature uniformity [47].

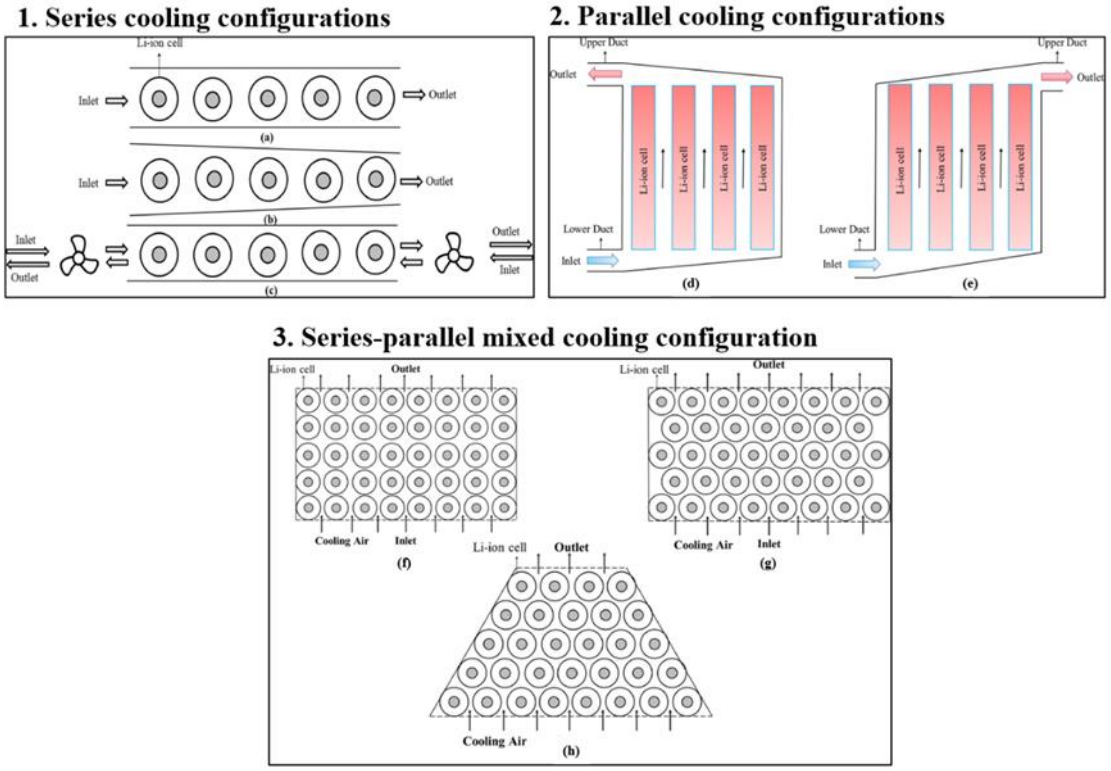

Figure 3.6 Configurations of air-cooling strategy: (a) Simple channel; (b) wedged channel; (c) simple channel with reciprocating cooling; (d) U- parallel configuration; (e) Z- parallel configuration; (f) Aligned bank; (g) staggered bank; (h) trapezoid configuration [48].

As for the impacts from parameter settings, Zhao conducted a rigorous assessment to investigate how these factors effect on the thermal management performance of the battery pack, including the ventilation types and velocities, gap spacing, number of single row cells, ambient temperature, cell diameter, etc [49]. The results showed that when air speed rose, the local temperature differential increased first and subsequently dropped. When deciding the gap spacing of

neighbor cells, configurations and cell's diameter should be taken into considerations. Also, the inlet pressure and velocity of the air were quite important parameters, directly influencing the maximum temperature of the battery and the power consumption. With increasing inlet pressure, the battery could get cooled down faster and its maximum temperature could be effectively reduced [50]. Similarly, with rising inlet velocity, the temperature uniformity got improved greatly [46], while the power consumption increased exponentially and the energy efficiency decreased simultaneously [51]. Besides, there was an upper limitation for the air-cooling capacity, which could be demonstrated by Fan's findings that the air-cooling capacity is proportional to the discharge rate with the increasing air inlet velocity [51]. Additionally, when the ambient temperature is too high, the power consumption increases and the battery temperature could rise to unsafe levels [5,49]. Thus, even air cooling distinguishes itself in many aspects such as the cost, complexity, maintenance, and weight, it is still not effective enough for power demanding applications or applications in high ambient conditions, which might be more suitable and available for more effective cooling strategies, like liquid cooling.

3.2.2. Liquid cooling

With relatively higher thermal conductivity and heat capacity, liquid cooling methods are able to meet the heat dissipation requirements of high-power battery packs and have been the mainstream of thermal management, saving parasitic energy up to 40% and lowering the noise level compared to air-cooling methods according to Roger Schmidt [46,52]. According to if the battery is with direct contact of circulated dielectric or not, liquid cooling methods can be classified as direct cooling and indirect cooling [48]. The former generally means that the battery entirely immersed in circulated dielectric to cool down all surfaces of every cell and improve temperature uniformity [53]. Based on its principle, the direct cooling is need of more rigorous sealing mechanisms and intricate integration to prevent coolant leakage. Also, the choice of the potential cooling media is of great significance, with the requirements of ensuring compatibility with cell components, avoid corrosion, and preserve long-term stability [46]. Chen made a comparison of commonly used cooling liquids of mineral oil and water/glycol coolant with air

cooling. Her results showed that even both liquid coolants were more thermally efficient than air cooling, they required a fairly low flow rate to seek a balance between pressure drop and power consumption due to their high viscosity [54]. Also, direct liquid cooling presents a spectrum of challenges, spanning from intricate system integration and potential leaks to electrochemical corrosion and electrical short [46]. Thus, the direct liquid cooling has not been widely applied used in BTMS of commercial EVs so far and more research have concentrated on the indirect cooling strategy, which is more practical [46,48].

As for indirect cooling, its cooling liquid flows through the heat sink attached at the surface of battery cells, whose cooling is influenced by the design of the heat sink, parameter settings, and the coolant selection. According to the configurations of the heat sink, indirect cooling is further classified as cold plate cooling, tube cooling, and jacket cooling, which are illustrated in **Figure 3.7**. For cylindrical cell, tube cooling is more typically used. Wavy tube has been applied in the BTMS of Tesla (**Figure 3.7** a), whose tube is made of aluminum coated with dielectric material to wrap the cell and is with the coolant of water-glycol mixtures [55]. The design of coolant jacket (**Figure 3.7** b) is more thermally effective and with better temperature uniformity than wavy tube because of the enclosed contact surfaces, while the wavy tube is safer from mechanical and electrical assessment and with lighter weight [46]. What is notable that the mini-channel cold plates (**Figure 3.7** d) and discrete tubes are specifically developed for prismatic cell [5]. Besides, the fin and cold plates can be combined to form an integrated heat sink, shown in **Figure 3.7** (e), and the metal fins can contribute to the heat dissipation from cells to cold plates [46]. For cooling plates, different types of coolant flow passages, seen in **Figure 3.8**, were studied, finding that by making angled incisions across the usual straight channel walls to disrupt the boundary layer can increase the heat transfer coefficient and the ideal flow channel design for greater temperature uniformity requires cross section of the channel to rise progressively with flow direction [56,57]. As for effects the from parameter settings, some factors including number of channels, flow direction, inlet mass flow rate, etc. also influence on the cooling results. For cold plate with mini-channels, Huo discovered that with higher inlet flow rate, the system is able to cool down

the battery more effectively and the optimal flow rate could be found [58]. Also, Jiaqiang proposed that the influence of channel number was most visible, followed by the effect of coolant flow rate, while channel height and width had the least effect when comparing their effects to heat dissipation [59]. To improve cooling efficiency of the liquid cooling methods, the improvement of liquid medium thermal property has been investigated. Water and aqueous ethanol are the most common choices for liquid cooling system coolant, but their low thermal conductivity actually limit the cooing efficiency. To solve this issue, Huo infused Al_2O_3 nanoparticles with water as the coolant, and the results showed that it did enhance the cooling performance and low the average temperature of battery [60]. Yang pushed it further, used liquid metal in BTMS, and found that it not only improved the temperature and uniformity cooling performance, but also consumed less parasitic power [61]. Considering the density of liquid metal is much larger than that of water, if ignore the drawback of a heavy cooling system, then liquid metal would be a better choice due to its excellent heat extraction and spreading capability [61].

With the advantages of high specific heat, great thermal conductivity, and high heat transfer coefficient, liquid cooling methods are regarded as a more practical and better choice for BTMS. However, their characteristics also lead to some questions including complexity in system design, higher costs, and potential threat from coolant leakage, which might damage the entire system and cause severe safety issues [48]. Thus, continued research and development are welcomed to solve mentioned problems and will definitely play a vital role in shaping the future of BTMS for LiBs.

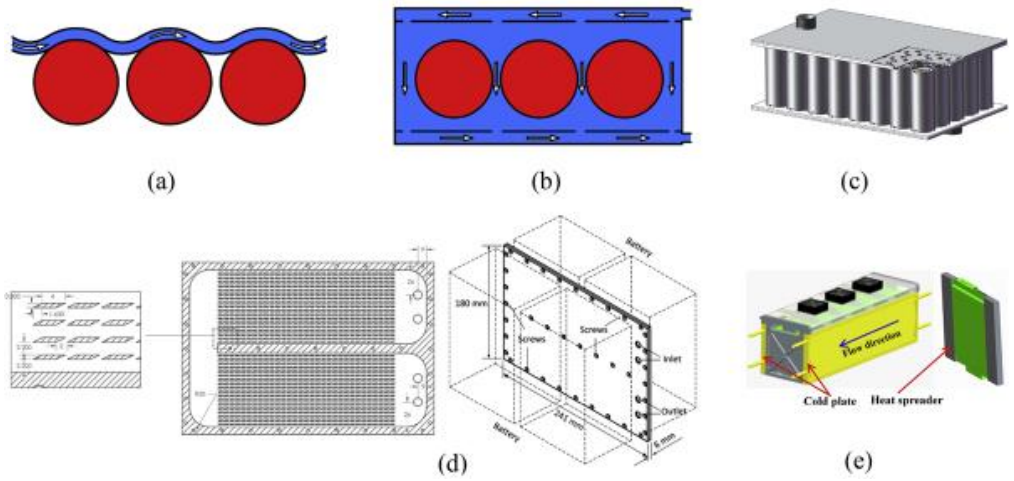

Figure 3.7 Different design of heat sinks. For cylindrical cells: (a) wavy tube; (b) coolant jacket; (c) liquid cooled cylinder. For prismatic cells: (d) cold plate with mini-channel; (e) combination of fin and cold plate with mini-channels [46].

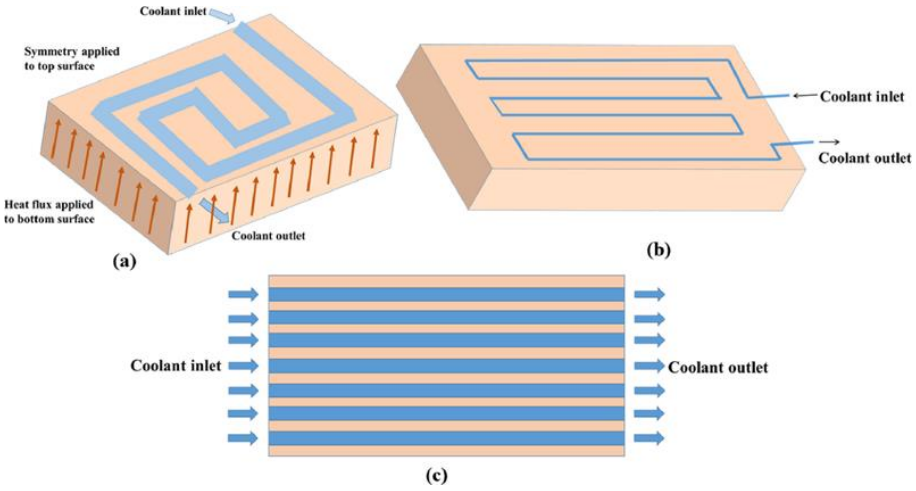

Figure 3.8 Different types of coolant flow path in cooling plate (a) Serpentine type; (b) U-type; (c) Multi-channel type [48].

4. Methodology

To avoid negative effects from extreme temperatures and achieve an effective BTMS, it is essential to understand the thermal behavior of the LiB and predict the temperature profile of the battery in operating conditions. Given the complexity and high expense of testing battery temperature and associated parameters in real automotives, an accurate thermal model of the LiB cell is critical for BTMS design and cell configuration optimization. Thus, a thermal model of LiB cell is developed, consisting of two parts: the heat generation model and the heat transfer model, which are elaborated in the following parts.

4.1. Heat generation model

Generally, the heat generation model of LiB cell can be categorized into three types: the black-box empirical models, the physics-based electrochemical models, and the equivalent circuit models (ECM) [62]. Based on empirical data collected from experiments, black-box models can establish mathematical relationships between input variables and the heat generation as the output only through some data-driven statistical estimation theories, such as artificial neural networks [63], with little knowledge of physical LiB system [64]. Even the black-box empirical models can get relatively accurate results in specific cases, it requires unacceptable computational costs and fails to be applicable in some situations, such as the temperature distribution of the internal components of LiB cell, if applied in the modelling of the heat generation. As for the electrochemical models, the most commonly used theory is physics-based Pseudo Two-dimensional (P2D) models, which used the concentrated solution theory and the porous electrode theory, developed by Newman's group in 1975 [65]. Regarded as one of the most typical models of battery cell, the physics-based electrochemical models are capable to provide insights into cell's performance and present a comprehensive description of the electrochemical phenomena occurring within the cell, and have continuously been developed and improved further since the P2D model, which helped to lower the computing cost to a large extent. However, its massive non-linear partial differential equations still cause the simulation to consume an

excessive amount of processing resources and is therefore limited by its own complexity [5]. Thus, among all the commonly used modelling methods, ECM is regarded as the optimal choice for its adequate precision and reasonable computational cost at the same time, making it widely adopted in heat generation model of LiB cell.

The equivalent circuit models are semi empirical models incorporating electrical circuit components including resistors, capacitors, voltage and current sources to depict the electrical characteristics of the battery cell [66]. Generally, the ECM can be classified into two categories: the Thevenin equivalent circuit model and the impedance based model, the method of which determining impedance model of a battery is called electrochemical impedance spectroscopy (EIS) [67]. Considering the lower expense and higher computation speed of Thevenin based model, the Thevenin equivalent circuit model is more suited and widely used in the prediction of battery performance [5].

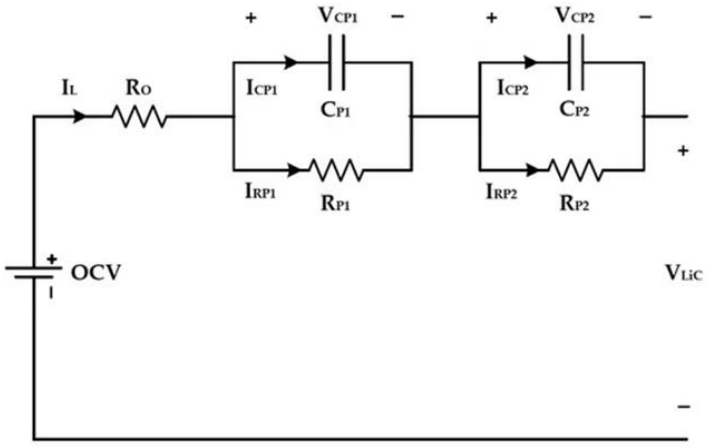

Figure 4.1 The second-order equivalent circuit model [68].

As shown in **Figure 4.1**, the second-order resistance and capacitance (2RC) ECM is applied in COMSOL Multiphysics 6.0 to calculate the heat generation. When a current is applied to the model, the output of the ECM is the estimated voltage response of the cell [68]. The open circuit voltage (OCV) can be represented by an ideal voltage source. R_0, like terminal resistance and electrode resistance, represents the internal resistance and is responsible for the instantaneous voltage changes during discharge and charge. C_i denotes the electrochemical double layer

capacitance [69]. This model includes 2 RC branches: the first describes the fast dynamics in the cell, presenting surface effects on the electrodes and reaction kinetics, while the second represents the slower dynamics of the cell.

Thus, the OCV *(*$\mathrm{E_{OCV}}$*)*, terminal voltage ($\mathrm{V_t}$), and current of each branch can be calculated as in [68]

$$\mathrm{E_{OCV}(SOC,T)} = \mathrm{E_{OCV,ref}(SOC)} + (\mathrm{T} - \mathrm{T_{ref}})\frac{\partial \mathrm{E_{OCV}(SOC)}}{\partial \mathrm{t}} \tag{4}$$

$$\mathrm{V_t} = \mathrm{E_{OCV}(SOC,T)} - \mathrm{IR_0(SOC,T,I)} - \mathrm{V_{C_{P_1}}(SOC,T,I)} - \mathrm{V_{C_{P_2}}(SOC,T,I)} \tag{5}$$

$$I_{RC_i} = \frac{V_i}{R_i} + C_i\frac{dV_i}{dt} \tag{6}$$

where $\mathrm{T_{ref}}$ means the surrounding temperature as a reference, I and $\mathrm{I_{RC_i}}$ represent the cell current and the current in polarization capacitance branches, C_P denotes the polarization capacitance, $V_{c_{p1}}$ and $V_{c_{p2}}$ are the voltage in the first and second polarization capacitance branches, respectively.

The electrical paraments of the developed model, encompassing ohmic and polarization resistances, as well as polarization capacitance, exhibit dependence on the state-of-charge (SOC) of the cell, the cell temperature (T), and current (I). Thus, these parameters are acquired by optimizing the voltage response of the second-order ECM against extensive lab tests on the cell. Once specific input parameters are set, including initial SOC, initial temperature, and initial capacity, the aforementioned electrical parameters can be calculated. The ECM comprises two look-up tables (LUTs) for OCV – one for charging and another for discharging. To represent the diverse operational conditions of vehicles, the second parameterization resistance (R2) entails two LUTs, corresponding to relax and slow dynamics states, while other resistances and capacitance solely possess a single LUT[70]. Based on following equation, the heat generated during the cell operation is mainly dominated by the reversible heat and the irreversible heat. Irreversible heat arises from various sources, such as concentration polarization, activation

polarization, ohmic polarization, and more. The irreversible heat is exothermic, meaning a heat loss all the time. Whereas the reversible heat is related to the entropy changes during chemical processes in cells, the sign of which alters according to the cell's SOC and current direction [62,71].

$$\dot{Q} = Q_{OCV} + Q_{R_0} + Q_{RC1} + Q_{RC2} = Q_{irr} + Q_{rev} \tag{7}$$

where $Q_{OCV}, Q_{R_0}, Q_{RC1}, Q_{RC2}$ represent the heat generated by different electrical components in ECM.

According to Bernardi et al. [71], the generation of heat of the total cell can be computed using the following equation:

$$Q = I(E - E_{\mathrm{OCV}}) + IT\left(\frac{\partial \mathrm{E}}{\partial \mathrm{T}}\right)_p \tag{8}$$

where E is the cell potential during the charge or discharge process, and $\left(\frac{\partial \mathrm{E}}{\partial \mathrm{T}}\right)_p$ is represents the temperature coefficient reflecting the entropy change.

The irreversible heat can be calculated as:

$$Q_{irr} = I(E - E_{\mathrm{OCV}}) = I^2 R_{\mathrm{in}} \tag{9}$$

where R_{in} stands for internal resistance, which is the key to calculate the irreversible heat.

Assumed that the absolute value of current flow in cathode and anode is almost the same, the reversible heat calculates as follows:

$$Q_{rev} = -IT\Delta S = IT\left(\frac{\partial \mathrm{E}}{\partial \mathrm{T}}\right)_p \tag{10}$$

Thus, the total heat generation of the full cell can be calculated according to equation (4) - (10).

4.2. Heat transfer model

Besides heat generation part, the heat transfer model constitutes another pivotal element within the thermal system of a cell. Depending on the extent of required prior knowledge concerning the physical system of the cell, heat transfer models are typically categorized as white-box, grey-box, and black-box models [64]. Each model is tailored to meet specific application requirements. Similar to the heat generation model, black-box heat transfer models can yield accurate temperature predictions with sufficient training data, albeit without the inherent physical significance of model parameters [72]. Due to its straightforward parameterization and ease of implementation, the lumped-parameter (LP) model, one of the most prominent grey-box models, is widely regarded as the optimal choice for real-time thermal management. However, this model's simplicity comes at the expense of simulating the temperature distribution within the internal components of the cell. However, when the finite element analysis (FEA) of the cell's internal structure is combined, a more comprehensive depiction of temperature gradients within the prismatic LIB cell becomes achievable. Building upon the LP model, the utilization of a Finite Element Model (FEM) that incorporates a detailed representation of the cell structure significantly enhances accuracy, even though it might entail higher computational demands [62].

Utilizing experimental measurements and the cell's physical properties, a 3D resolved thermal model with detailed cell structure was developed. This model encompasses the complete cell structure, encompassing the tabs' frame, the positive and negative current collectors, the stack, the cell's cap, cap insulation, outer tapes, and the can, which is shown in **Figure 4.2**. Utilizing the computational domain mentioned above for the numerical simulations, the mesh for the cell is approximately composed of 31K tetrahedron elements for the real geometry (**Figure 4.3**) with an average quality of 0.5603. Within the domain, the maximum and minimum element sizes are 23.4 mm and 4.21 mm, respectively. Besides, tabs experience heating due to the diffusion of heat generated within the cell.

Given the unavailability of material characteristics inside the cell, joule heating in the tabs has been disregarded in the current simulations.

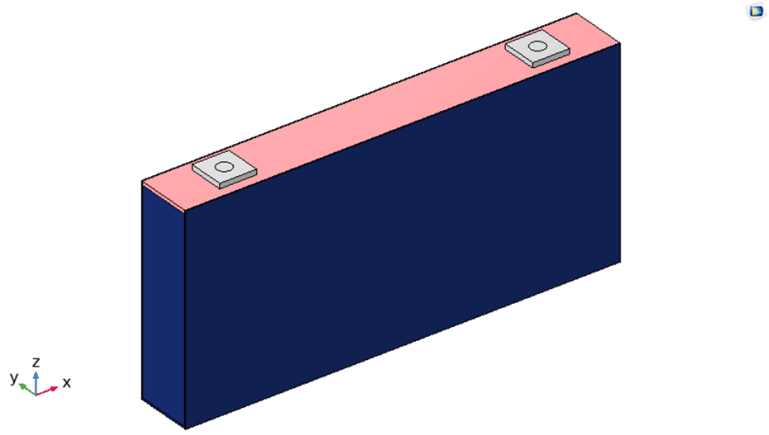

Figure 4.2 The view of 3D resolved thermal model

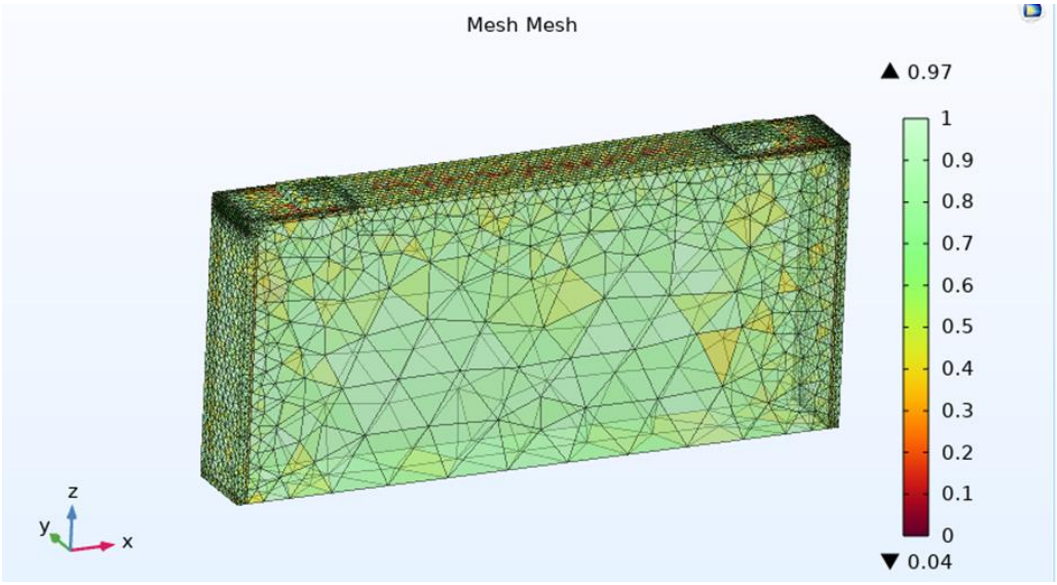

Figure 4.3 Geometry of the cell.

To describe the conduction that happened in the internal cell during cycling, the heat transfer in solids and fluids module was used in COMSOL. The heat transfer process is delineated through the following part [73].

As for the heat transfer in solids,

$$\rho C_p \frac{\partial T}{\partial t} + \rho C_p \mathbf{u} \cdot \nabla T + \nabla \cdot \mathbf{q} = Q + Q_{ted} \quad (11)$$

For heat transfer in fluids:

$$\rho C_p \frac{\partial T}{\partial t} + \rho C_p \mathbf{u} \cdot \nabla T + \nabla \cdot \mathbf{q} = Q + Q_p + Q_{vd} \quad (12)$$

$$\mathbf{q} = -k\nabla T \quad (13)$$

In its basic form, the density ρ, heat capacity C_p, thermal conductivity k, heat sources Q, Pressure work Q_p,viscous dissipation Q_{vd}, constraint temperatures T, and heat fluxes $\mathbf{q}$. Considering not all parameters are constant, which leads to a nonliner system.

With Dirichlet and Neumann boundary conditions at some boundaries,

$$-\mathbf{n} \cdot \mathbf{q} = q_0 \quad (14)$$

$$q_0 = h(T_{ext} - T) \quad (15)$$

Where $\mathbf{n}$ stands for the normal vector toward exterior.

Additionally, in relation to the boundaries of the cell's six surfaces exposed to the surroundings, a thin layer concept was employed to simplify heat transfer process for packaging layers such as the can and tapes. This concept revolves around the idea of replacing micro-scale layers in the object geometry with heat transfer resistance terms to avoid the burden of computation for exceedingly thin layers. This ensures that the temperature at any point within this thin layer is equivalent to the temperature at points situated on the thermal insulation layers with substantial thickness. As shown in **Figure 4.4**, the thin layer was indicated with a light blue color, with a specific point A situated on its boundary interface. Additionally, at the boundaries of other thermal insulations with certain thickness,

there was another point labeled as B. The utilization of the thin layer ensured that the temperature at points A and B are identical $(T_A = T_B)$, thereby establishing temperature consistency and simplify the heat transfer process through this approach.

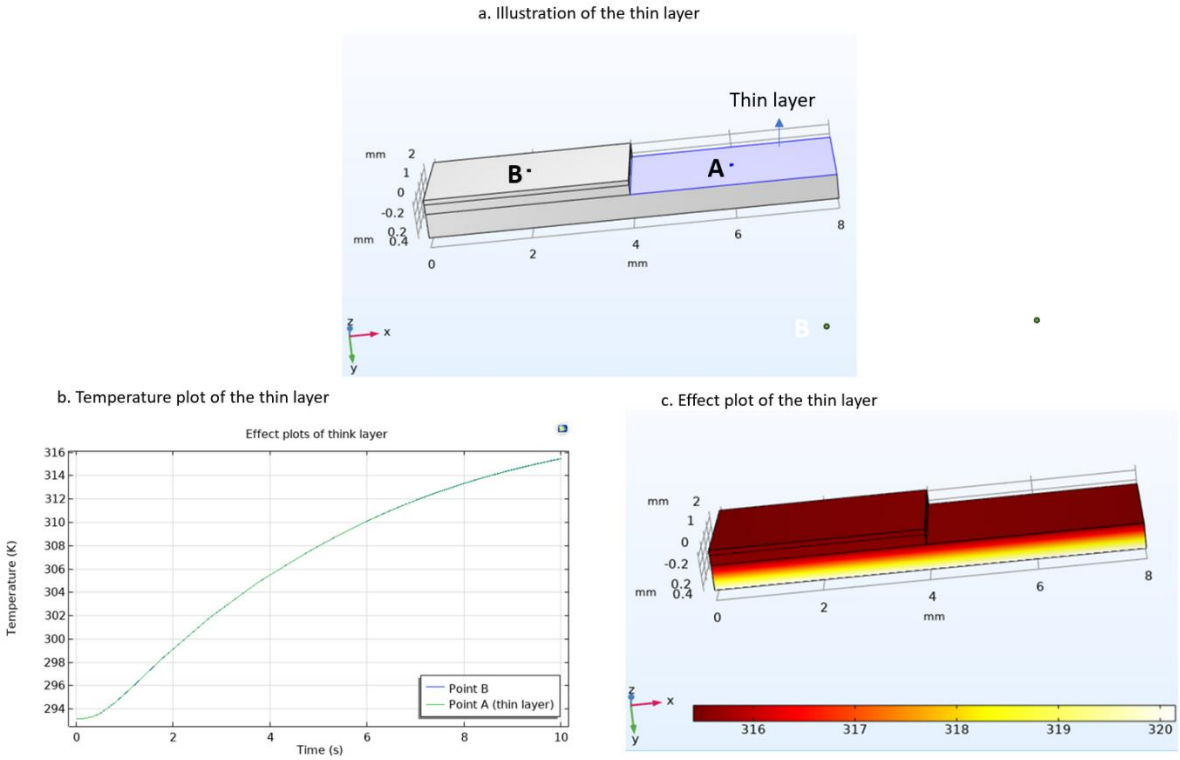

Figure 4.4 Illustration of thin layer concept.

4.3. Model outline

The coupled electro-thermal model is established and its schematic representation is depicted in **Figure 4.5**. By utilizing input data concerning the cell's characteristics, relevant electrical parameters, and temperature records, the developed model is capable of predicting the internal temperature distribution and voltage response of the cell based on the applied load cycle. As elaborated above, this model encompasses two sub-models: the heat generation model based on a 2RC-ECM and the heat transfer model based on the cell's geometry utilizing FEA.

Primarily, the heat generation was calculated, which encompasse the irreversible heat generated by Joule heating and the reversible heat attributed to

entropy change, through the ECM. Subsequently, this calculated heat generated by the cell was then distributed across its internal components in accordance with its structural composition. The governing equations for heat generation and heat transfer were discretized for the constructed cell geometry using the finite element method. These equations were subsequently solved through COMSOL with the fully coupled time-dependent solver. The computational process employed a time step of 1 second.

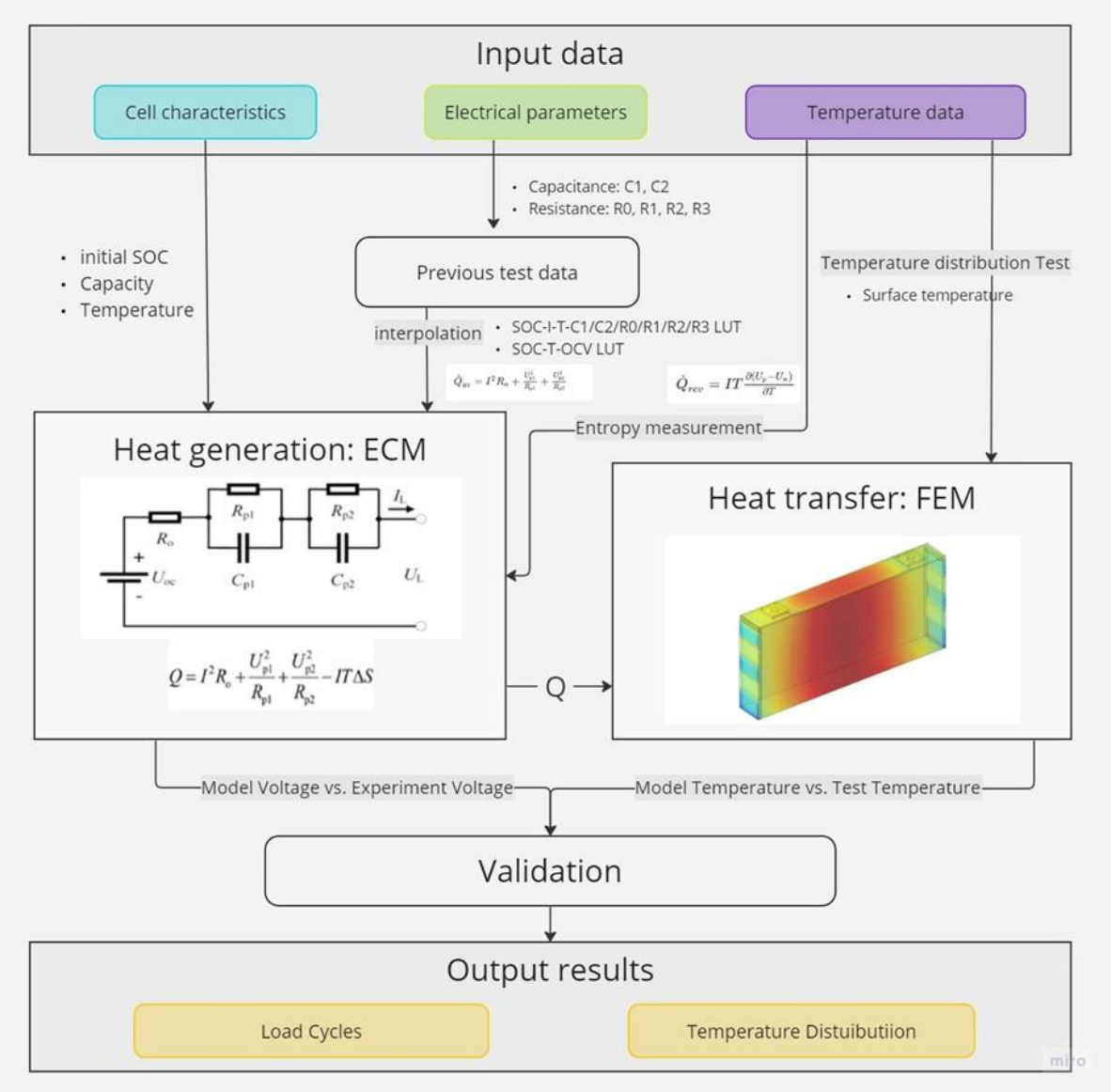

Figure 4.5 Schematic illustration of the electro-thermal 3D model

4.4. Experiment

This section outlines the design and setup of two experiments. The temperature distribution test, wherein temperature fluctuations are measured at various points across each surface of the cell. This test aims to validate and visually depict the temperature distribution across the cell's surface. The second experiment concerns the measurement of the entropy coefficient, which is conducted to obtain the entropy profile, a crucial factor in calculating the reversible heat.

4.4.1. Cell characteristics

All measurements were carried out on single cell. The cell under study is a prismatic lithium-ion cell that utilizes graphite anode and nickel rich cathode. It possesses a nominal capacity of 150 Ah. The upper and lower cut-off voltages for this cell are set at 4.2 V and 2.8 V, respectively. Other detailed characteristics are shown in **Table 4.1**

Table 4.1 Investigated cell characteristics.

Maximum voltage/ V	4.2
Minimum voltage/ V	2.8
Nominal capacity/ Ah	150
Type	Prismatic
Chemistry	Graphite anode - Nickel rich cathode

4.4.2. Temperature distribution test

To comprehensively elucidate heat transfer and temperature fluctuations from points to points, this experiment was structured to visualize temperature distribution across the cell surface and validate simulation outcomes.

The experimental setup utilized a total of 40 K-type thermocouples, with the distribution as follows: 9 thermocouples on both the front and back surfaces (**Figure 4.7 a**), 3 thermocouples on each of the remaining four surfaces, and 2 thermocouples in each of the five directions exposed to the air, except for the downward-facing bottom sides, illustrated in **Figure 4.6**. The cell was placed within a thermal insulated box, enhancing the ability to closely monitor temperature fluctuations. The experiment equipment used in the temperature distribution test (shown in **Figure 4.7 b**) was a an MACCOR 4000 with 0.02% of full-scale voltage, 0.05% full-scale current, and 16-b resolution. The thermal box containing the cell was put inside the climate chamber of LaboTest PGX-224, setting the surrounding temperature at 25 ℃ during the test.

The complete test procedure can be found in **Appendix 8.1 Temperature distribution test**. The cell underwent a discharge process until reaching 0% SOC prior to entering the pulsing cycles utilizing a current of 1/3 C, which is an appropriate current magnitude, strikes a balance between not being too high to overlook entropy heat and not being too low to miss observing joule heat. Subsequently, within a loop comprising 10 consecutive cycles of full charging and discharging with the range of 0 to 100% SOC, the temperature at various sites on the cell was recorded.

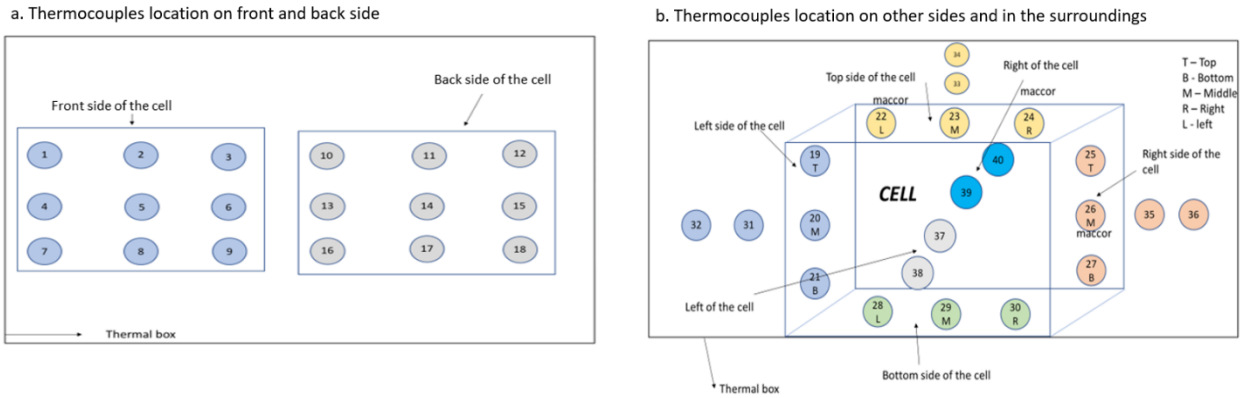

Figure 4.6 The design of thermocouples sites on the large surfaces of the cell (a) and the rest (b).

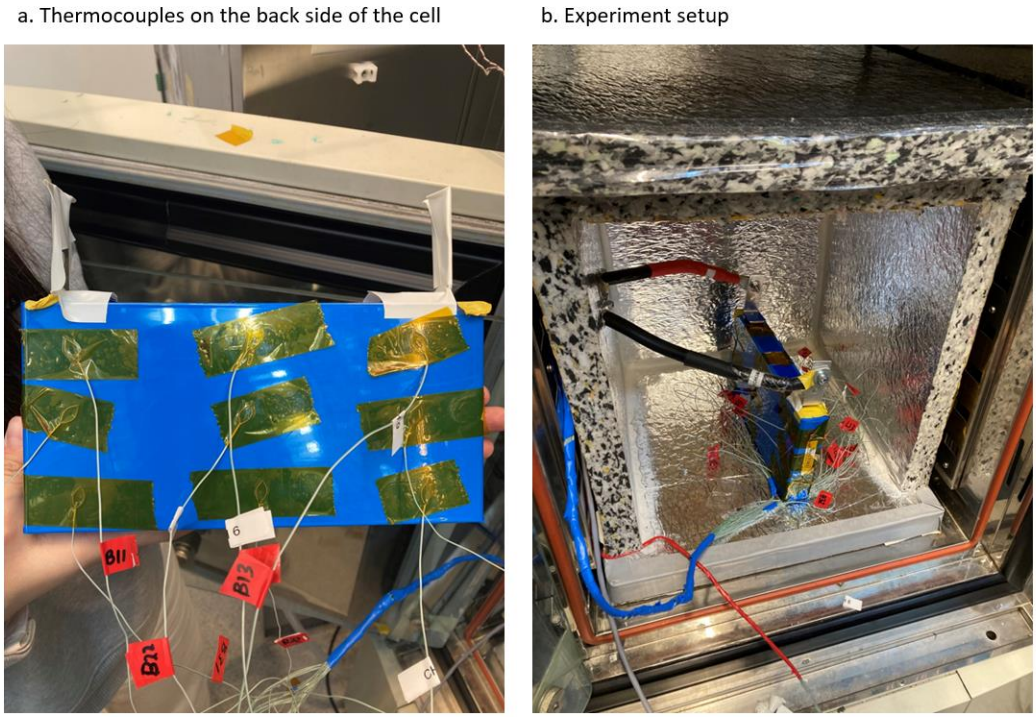

Figure 4.7 Thermocouple sites on cell's back side (a) and the experiment setup (b).

4.4.3. Entropy coefficient measurement

According to equation (8) - (10), entropy changes exert a significant impact on cell temperature, particularly evident at low C rates. Consequently, incorporating entropy changes is imperative to enhance the accuracy of the thermal model employed.

The entropy profile is commonly determined through several methods, notably potentiometric, frequency-domain, and calorimetric approaches [74–76]. Calorimetric methods, in general, function by quantifying the total heat generated with a calorimeter, segregating reversible and irreversible heat components from the total, and subsequently deriving the entropic coefficient from the part of reversible heat. While the calorimetric method offers entropy profile across the entire SOC range relatively fast, it encounters certain obstacles when applied to larger cells such as the targeted cell in this project. These obstacles encompass the high cost of the calorimeter equipment and the potential fire hazards they pose [76,77]. Another approach, exhibiting enhanced accuracy, is the frequency-domain technique termed entropy change via electrothermal impedance spectroscopy (EIS). This method operates by utilizing known thermal impedance and measuring surface temperatures to derive internal heat flow within the cell, which is a linear function of current and entropy change [77]. Although this method presents itself as a highly appealing way of entropy measurement, offering a balance between fast data acquisition and precision, it necessitates a significant investment of time and effort in the pre-processing of data to achieve satisfactory results. Thus, this project has opted for one of the most typical and reliable approaches, the potentiometric method introduced by Thompson [78]. This method involves the direct measurement of the OCV at varying temperatures after a relaxation interval. Despite its slightly longer measuring time compared to others, the potentiometric method ensures the accuracy of the entropy profile and significantly contributes to the development of a highly precise heat transfer model.

The potentiometric test (shown in **Figure 4.8**) is powered by the same system as the temperature distribution test. The temperature is controllable by the programmable climate chamber Weisstechnik C/600/70/3 recorded with 3 type K thermocouples, the site of which are near positive and negative tab, as well as the center of the left side. In this measurement, it is the temperature change ΔT that affects the result but not the absolute temperature.

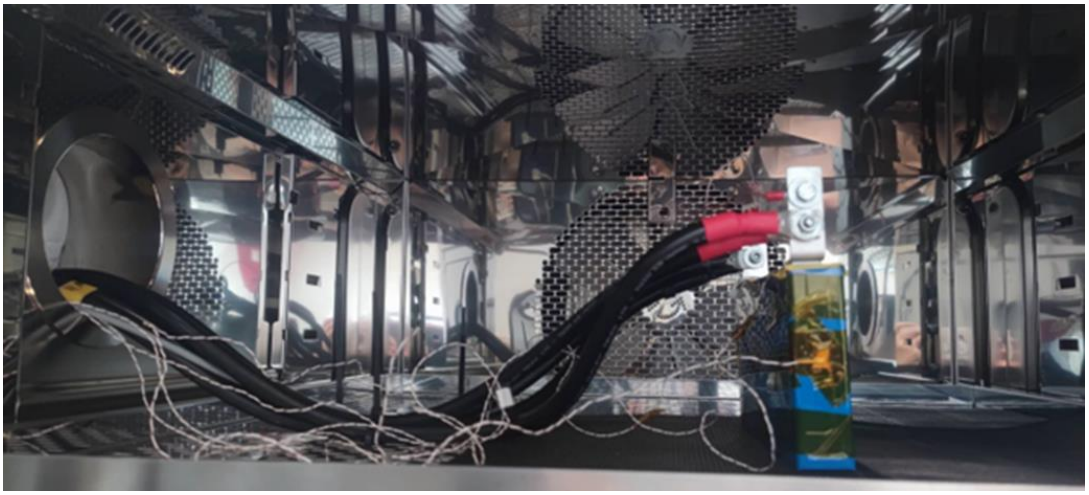

Figure 4.8 The setup of potentiometric method for entropy measurement.

Followed the method mentioned in [76], the test procedure can be seen in **Appendix 8.2 Entropy coefficient measurement**, showing that the entropic coefficient was assessed across 10 SOC levels, ranging from 100% to 10%, with intervals of 10% SOC. What need to notice was that measurements were not conducted at 0% SOC, reaching this state is rare in realistic scenarios and can lead to certain cell performance issues. The measurement commenced with the cell being fully charged to 100% SOC. Subsequently, it was discharged to the next SOC level at a rate of 0.33C for a duration of 40 minutes. Following each discharge cycle, the cell was relaxed for 4 hours at each designated temperature. Temperature conditions were regulated within a controlled environment provided by the climate chamber, with temperatures varying from 30°C down to 10°C in increments of 10°C. The voltage of the cell at last period of the relaxation was regarded as cell's OCV at each temperature for every SOC level.

5. Results and discussion

5.1. Test Results

5.1.1. Surface temperature distribution

The voltage, current, and other electrical parameters of the cell during the temperature distribution test were presented in **Figure 5.1** and **Figure 5.2**. In terms of the temperature variations at different sites on the cell, **Figure 5.3** depicted the temperature changes on the front side. The other thermocouples were plotted as the delta towards the middle one. There are 9 graphs corresponding to the site of thermocouples on the front surface, demonstrating a consistent trend with slight variations (maximum temperature difference were only 0.5 ℃) among different locations. Left side (**Figure 5.4**) and the remaining four surfaces were observed with similar results.

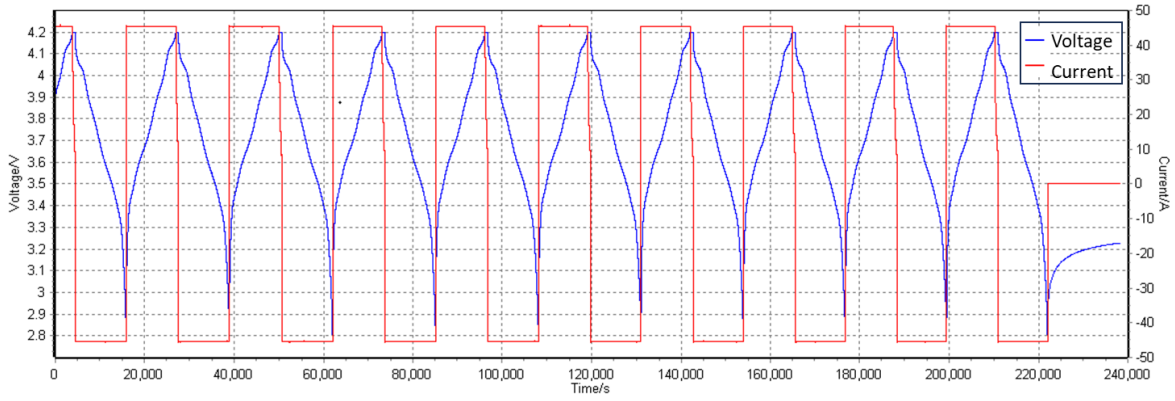

Figure 5.1 Voltage and current during temperature distribution test.

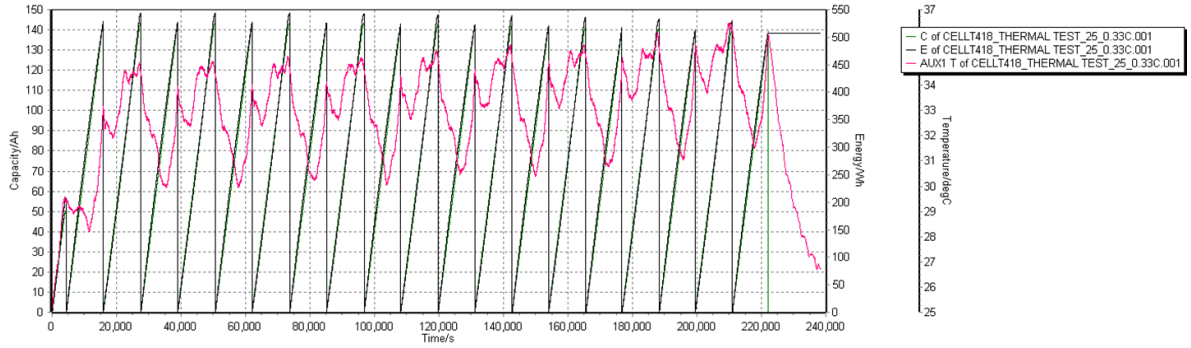

Figure 5.2 Capacity, energy, and temperature during temperature distribution test.

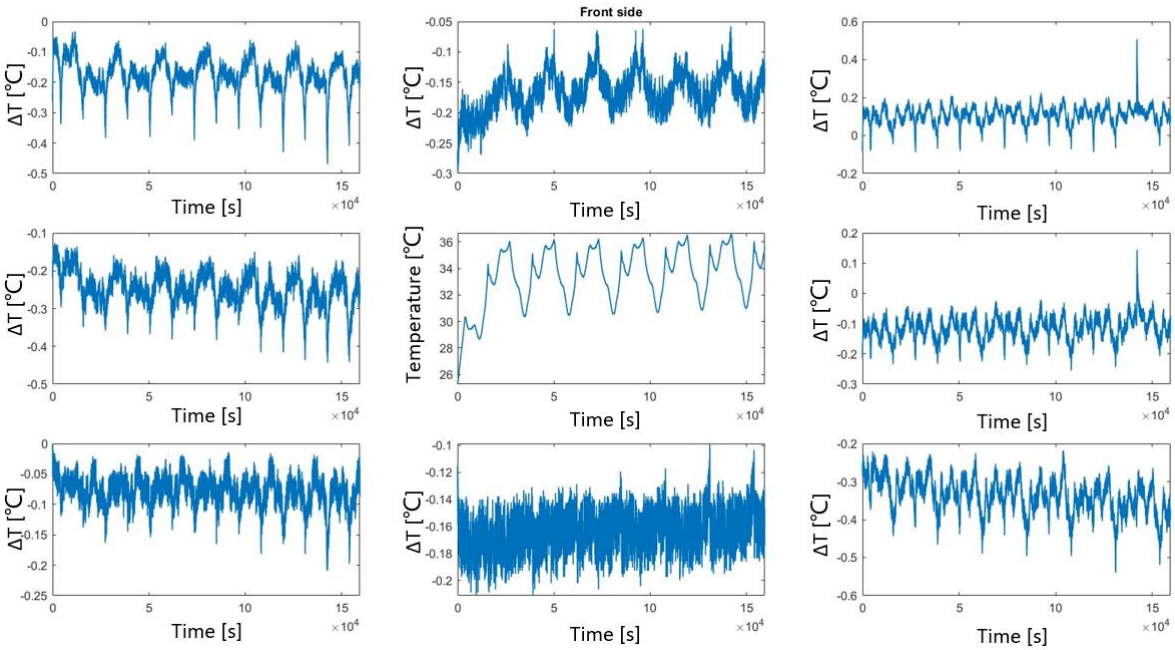

Figure 5.3 Temperature of front surface of the cell.

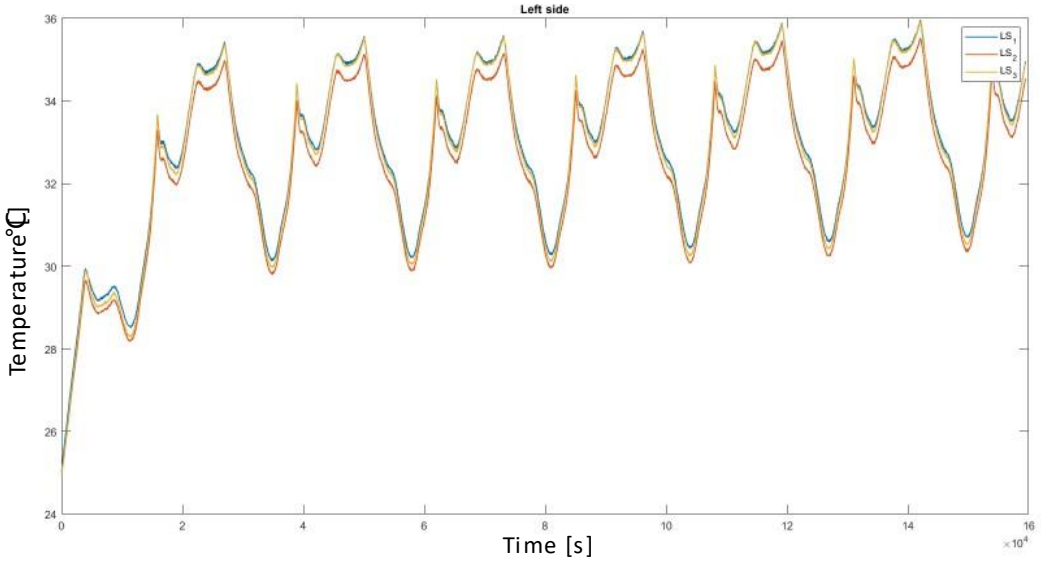

Figure 5.4 Temperature of left surface of the cell.

5.1.2. Entropy profile

The voltage and current profiles observed during the entropy coefficient measurement were illustrated in **Figure 5.5**, and the variations in energy, capacity,

and temperature were depicted in **Figure 5.6**. Based on the graphs mentioned, the OCV values were obtained at 3 designated observation temperatures within the SOC range spanning from 100% to 10%. The gradient of these OCV points at different temperature illustrated the entropy coefficient.

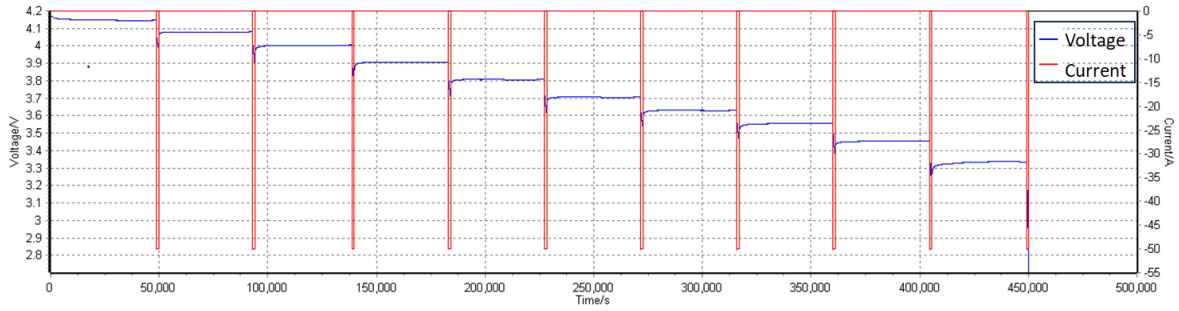

Figure 5.5 Voltage and current during entropy measurement.

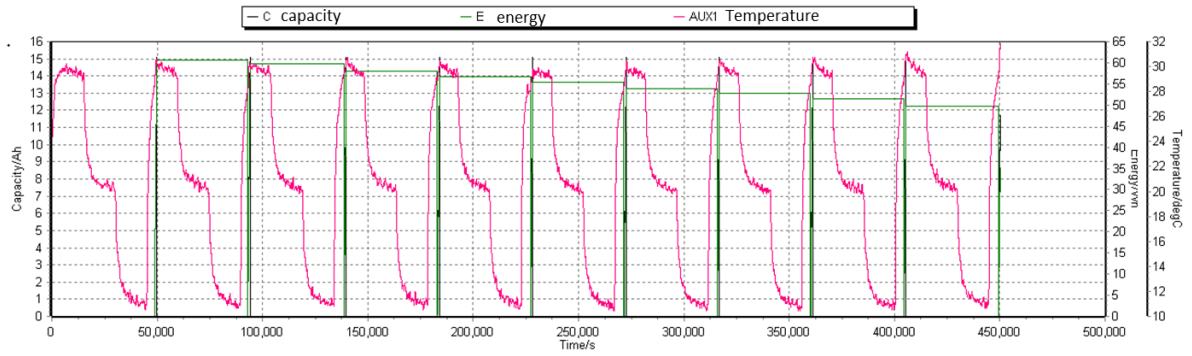

Figure 5.6 Temperature variation during entropy measurement.

Recognizing that the 10 data points from discharge side obtained from the experiment might not provide sufficient accuracy for the reversible heat. The outcomes cited in [79], which employed the same electrode materials and analogous chemistry as the cell utilized in this project, were integrated to elaborate upon the entropy profile for both discharge and charge sides. These results are depicted in **Figure 5.7**. The red dots represented the experimental data, while the black dots represented the reference data. Both sets of data exhibited similar entropy profiles, with the reference data offering more detailed variations in entropy coefficients and data from the charge side. This enhanced dataset for entropy contributes to a more accurate calculation of reversible heat.

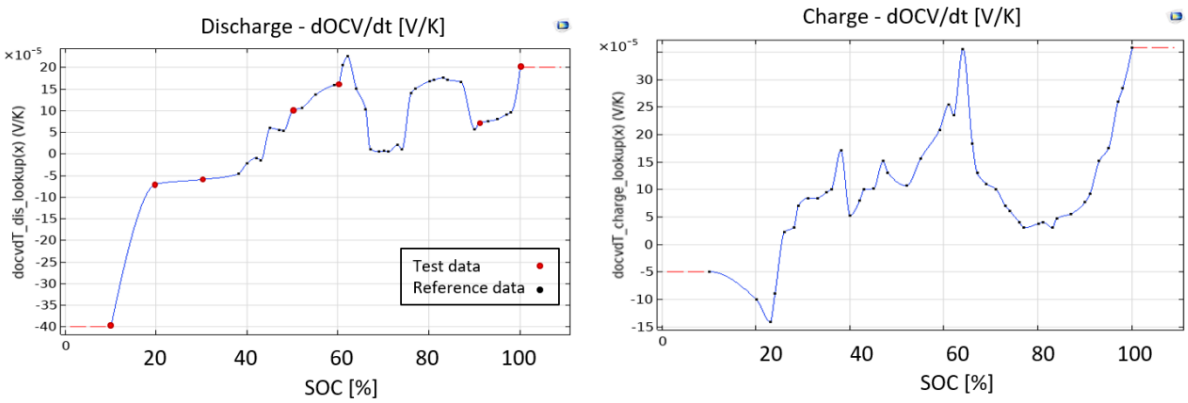

Figure 5.7 Entropy coefficient as function of SOC for the charge and discharge.

5.2. Model validation

5.2.1. Heat generation model validation

Considering ECM is developed based on electrical parameters of the cell, such as ohmic, current, polarization resistances, etc., voltage is determined as the factor to validate the developed 2RC-ECM. A series of diverse types and levels of current was applied in the model to mimic different operation scenarios of the cell, during which, the error of the test voltage and simulated voltage were calculated to estimate the ECM performance.

$$\text{Voltage Error} = \frac{|\text{Experiment Voltage} - \text{Model Voltage}|}{\text{Experiment Voltage}} \times 100\% \quad (16)$$

In ECM, SOC works an important parameter, because it enables to make the bridge between cell's voltage and its heat generation, displaying as cell's temperature, providing valuable information about the capacity, energy and performance of the cell. **Figure 5.8** shows the OCV–SOC-Temperature curve when charging and discharging current was applied.

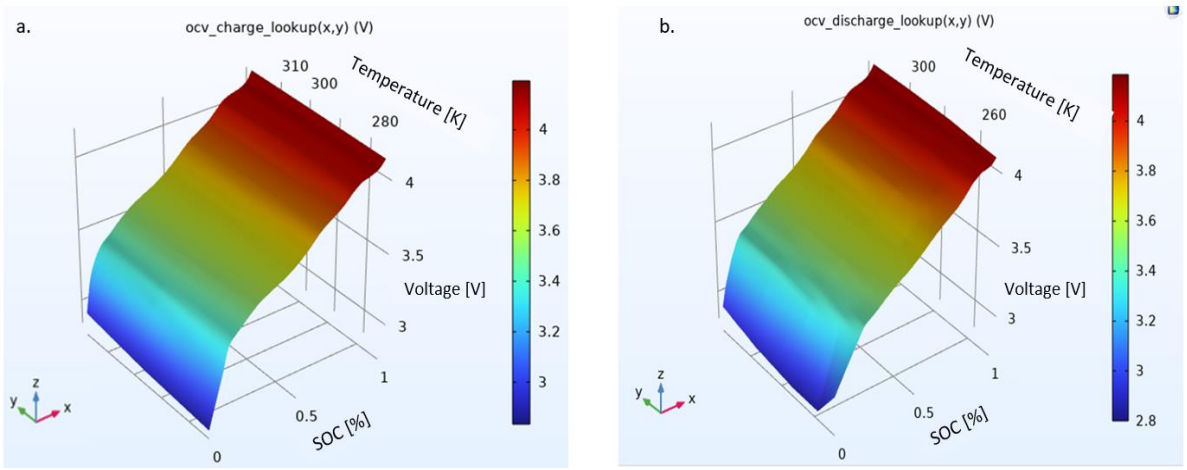

Figure 5.8 The test curve for OCV-SOC-Temperature of the cell of (a) charging current and (b) discharge current.

Based on the initial parameters of input data and the interpolation of LUTs, the terminal voltage and the heat generation of the cell were calculated according to Equation (5) and Equation (7) -(10).

Figure 5.9 to **Figure 5.12** revealed the results of the developed 2RC-ECM through voltage validation from simple current cycles to dynamic cycles of different current levels correspondingly, **Figure a** of which displayed the detailed comparison of test voltage and simulated voltage, while **Figure b** depicted the error of the measured and model results. As for the simple load cycles (**Figure 5.9**), the voltage error was all below 2%, demonstrating a fairly dependable model for heat generation. As for dynamic current cycles, 3 different levels current were applied and lasted for longer periods, varied from high current of 1C to the medium current of 1/3C, then to low current of 1/10C. It is noteworthy that the direction of current displaying in COMSOL is opposite of the reality, which means that the positive current is actually discharging current. As for high current, voltage errors were also less than 2% except one breaking point reached around 6%, which was the switch point for the current direction as well as the change of charge and discharge LUTs. At medium current, a parallel trend was observed in comparison to the high current scenario, where a maximum voltage error of approximately 5.5% emerged at the point of transition between current direction. In the low current group, model results closely aligned with test ones and the voltage error

were uniformly below 2.5%. The model underwent a series of dynamic fast-charging cycles to mimic real-world automotive conditions. The outcomes of these cycles are depicted in **Figure 5.13**, revealing a maximum voltage error of 5.5% at the cycle's initial part. Moreover, it's important to highlight that the model exhibited relatively less accuracy when discharging to low SOC compared to other situation. Results of these groups showed some similarities: the maximum voltage error point usually appeared at the current direction switch point, but it did not affect the high accuracy and excellent performance of the ECM.

After sets of validations comprising high, medium, low current and fast charging scenarios, the results revealed the excellent performance and reliability of ECM in simulating dynamic driving cycles. Therefore, the ECM can be able to integrate with heat transfer model for further research.

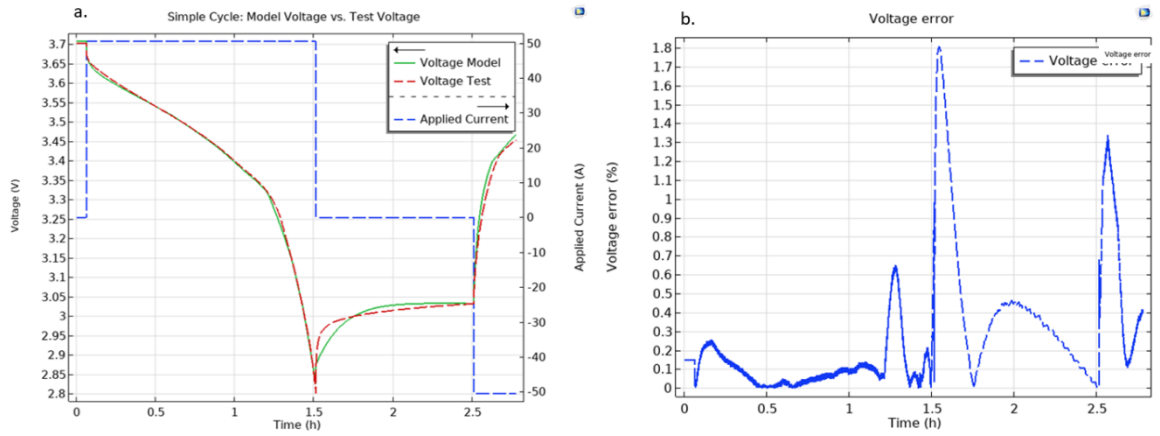

Figure 5.9 Validation of ECM for simple current cycles: (a) verification of the simulation and experimental results of voltage, (b) error of voltage.

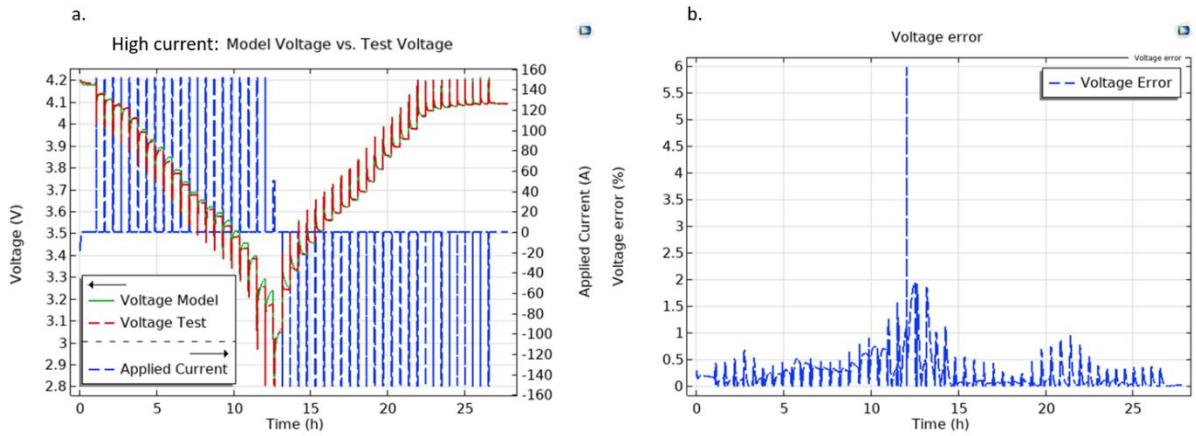

Figure 5.10 Validation of ECM for high level dynamic current cycles: (a) verification of the simulation and experimental results of voltage, (b) error of voltage.

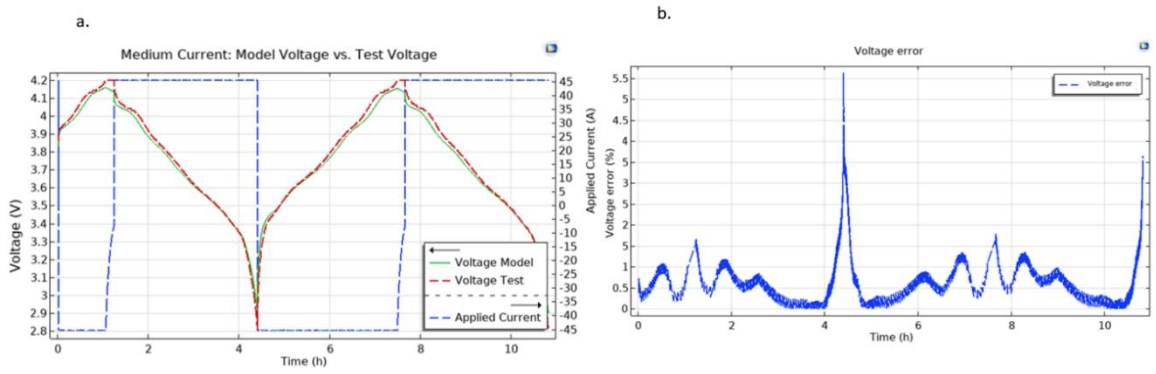

Figure 5.11 Validation of ECM for medium level dynamic current cycles: (a) verification of the simulation and experimental results of voltage, (b) error of voltage.

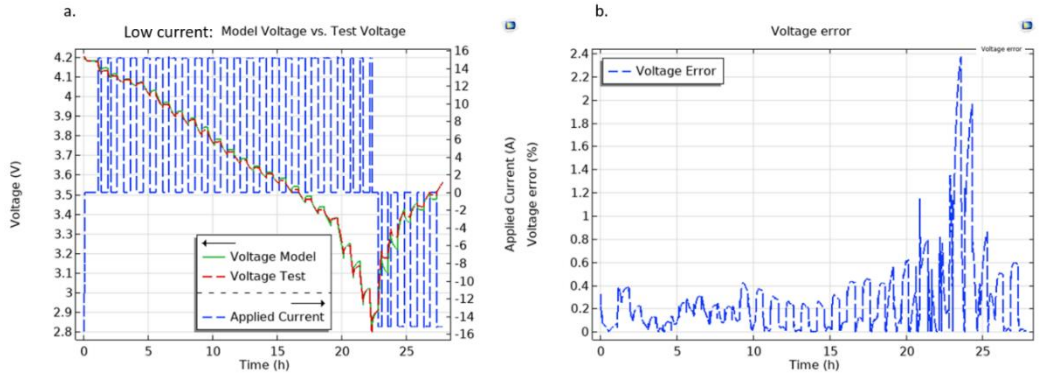

Figure 5.12 Validation of ECM for low level dynamic current cycles: (a) verification of the simulation and experimental results of voltage, (b) error of voltage.

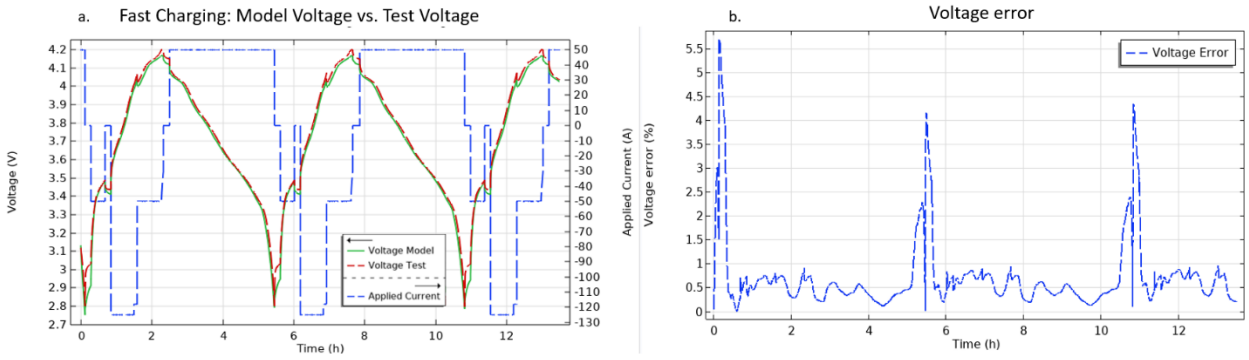

Figure 5.13 Validation of ECM for dynamic fast-charging cycles: (a) verification of the simulation and experimental results of voltage, (b) error of voltage.

5.2.2. Heat transfer model validation

In order to validate the FEA heat transfer model, a medium-level current (1/3C, approximately 45A) was applied to the model, and the load cycle results were consistent with those depicted in **Figure 5.11** It was this particular C rate of the current that was deliberately selected to effectively showcase the heat generated from both Joule heating and entropy. The average temperature for each surface as well as the individual temperature at various sites on those surfaces were used. By comparing the difference between the model and experiment data though calculating the temperature error, the accuracy of the model could be estimated and assessed.

$$\text{Temperature Error} = \frac{|\text{Experiment Temp.} - \text{Model Temp.}|}{\text{Experiment Temp.}} \times 100\% \quad (17)$$

The results, from **Figure 5.14** to **Figure 5.19**, illustrated the outcome of surface average temperature validation through the assessment of temperature errors. Similarities were observed in the results for each surface. The model's outcomes adeptly replicated the trends in temperature variations as the experiment group, substantiated by errors that all remained below 0.75%. Although subtle discrepancies from the experimental data occasionally emerged in specific peak and valley values.

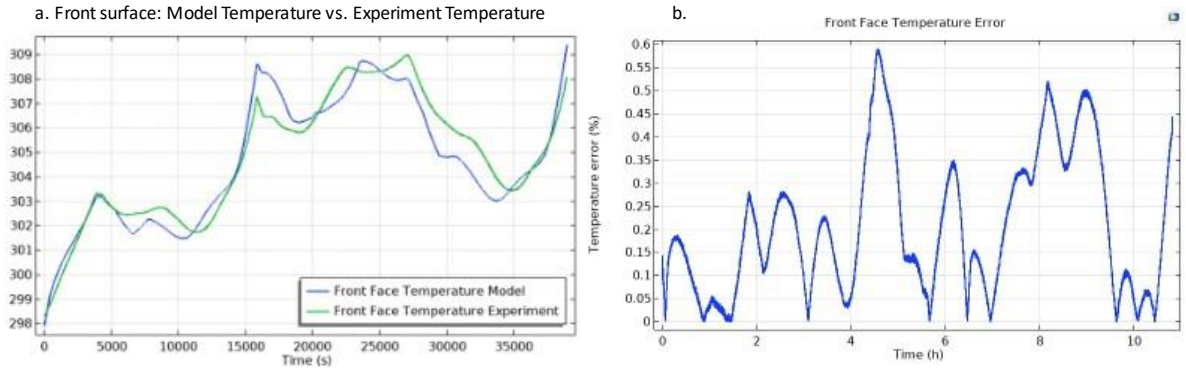

Figure 5.14 Validation of FEM for front surface: (a) verification of the simulation and experimental results of average front surface temperature, (b) temperature error.

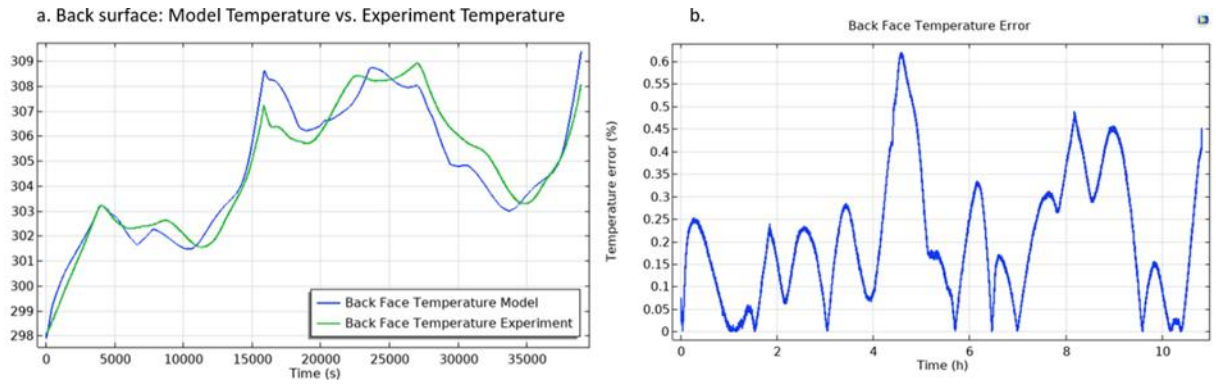

Figure 5.15 Validation of FEM for back surface: (a) verification of the simulation and experimental results of average back surface temperature, (b) temperature error.

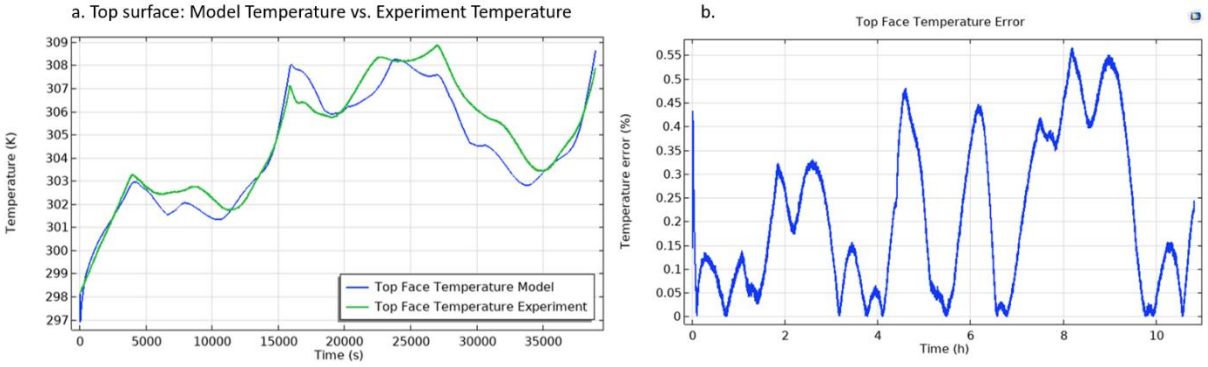

Figure 5.16 Validation of FEM for top surface: (a) verification of the simulation and experimental results of average top surface temperature, (b) temperature error.

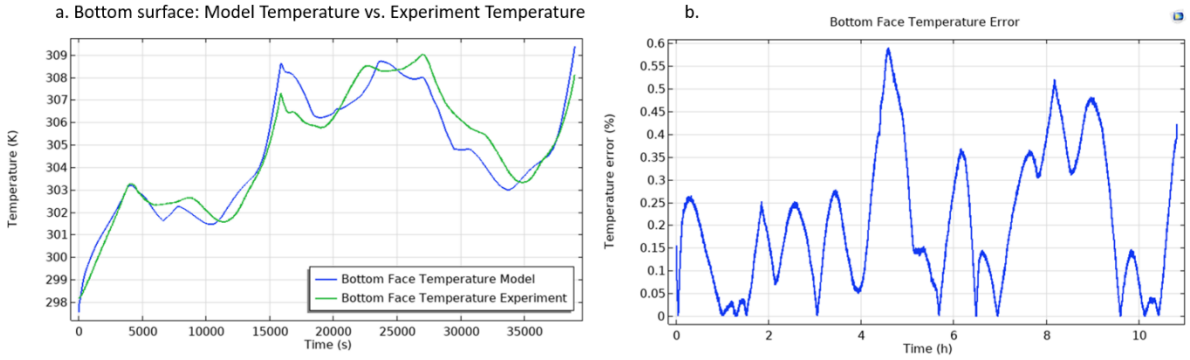

Figure 5.17 Validation of FEM for bottom surface: (a) verification of the simulation and experimental results of average bottom surface temperature, (b) temperature error.

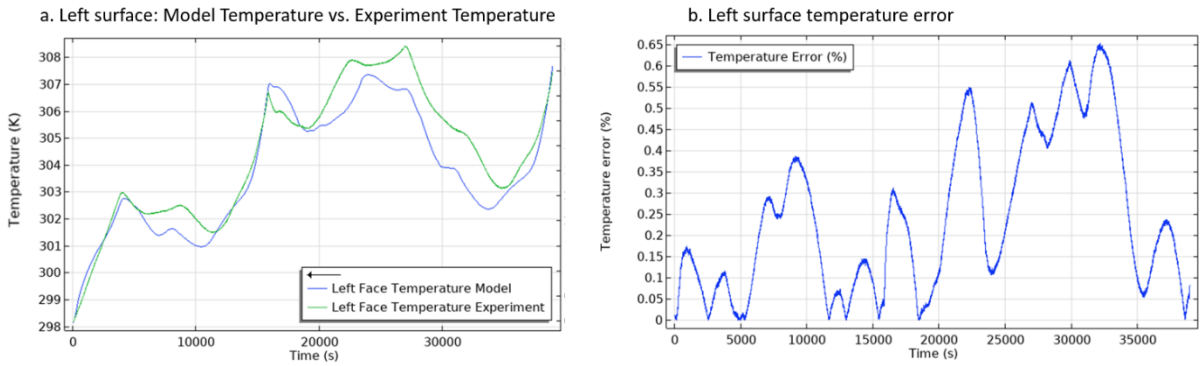

Figure 5.18 Validation of FEM for left surface: (a) verification of the simulation and experimental results of average left surface temperature, (b) temperature error.

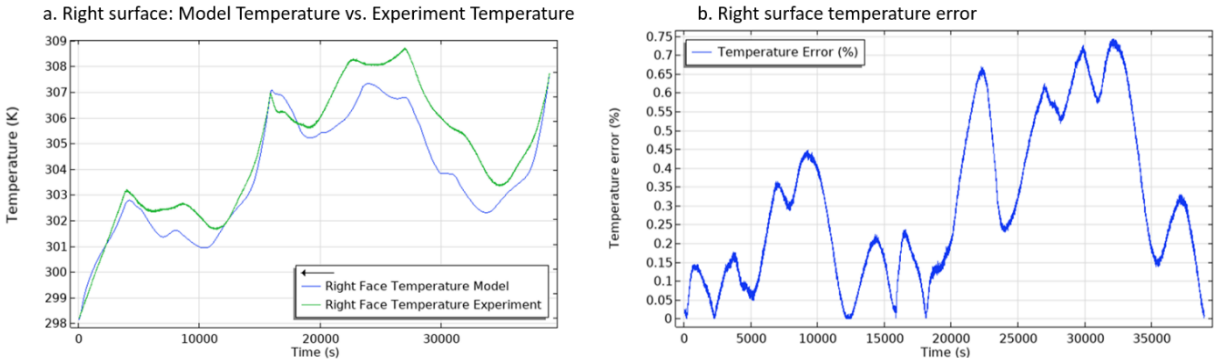

Figure 5.19 Validation of FEM for right surface: (a) verification of the simulation and experimental results of average right surface temperature, (b) temperature error.

Taking into account the considerable number of temperature points across each surface, one temperature sampling point was selected for each surface to compare the model's temperatures with experimental measurements, seen in **Figure 5.20** to **Figure 5.25**. The temperature data for each surface continued to exhibit similar trends, akin to its average surface temperature. It's worth noting that, regarding points' temperature, the maximum temperature error reached 0.8%, slightly higher than the error observed for the average surface temperature. This divergence can be attributed to disparities between the placement of thermocouples and the selection of temperature points within the model, leading to differences in the results.

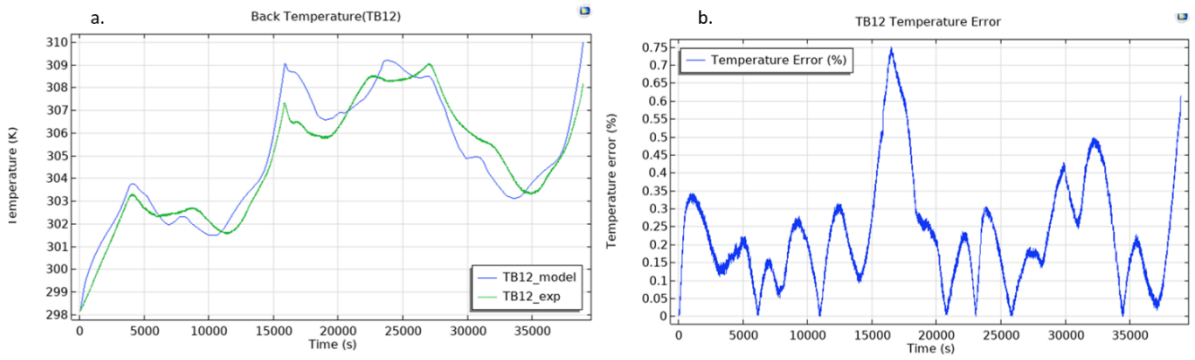

Figure 5.20 Validation of FEM: (a) verification of the simulation and experimental results of TB12 on the front surface, (b) temperature error.

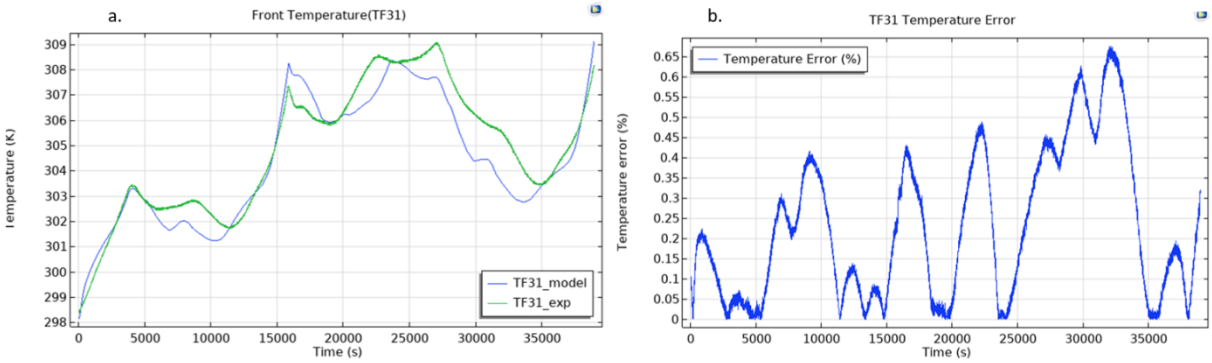

Figure 5.21 Validation of FEM: (a) verification of the simulation and experimental results of TF31 on the back surface, (b) temperature error.

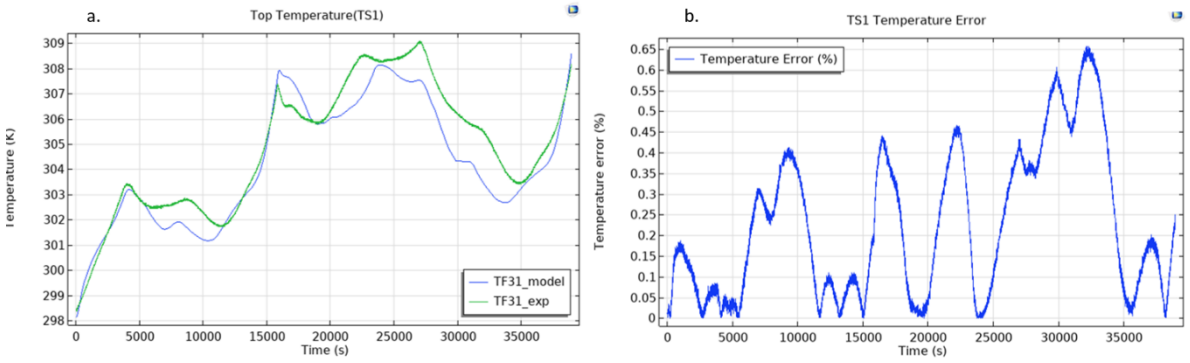

Figure 5.22 Validation of FEM: (a) verification of the simulation and experimental results of TS1 on the top surface, (b) temperature error.

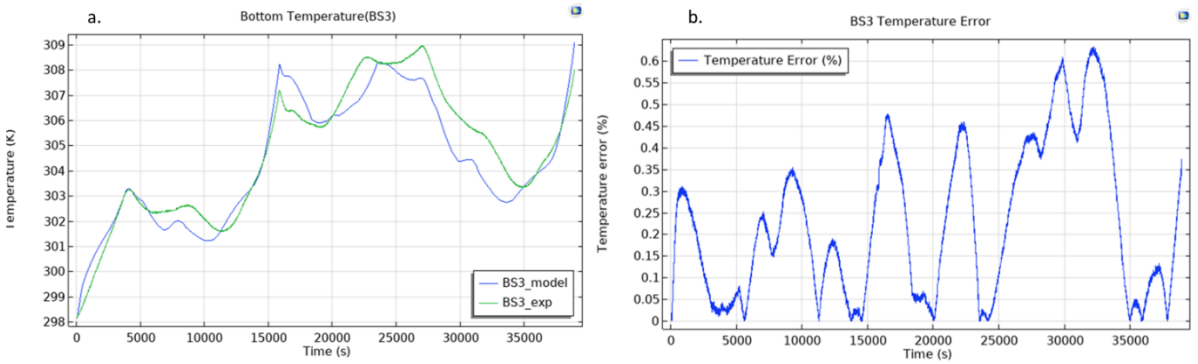

Figure 5.23 Validation of FEM: (a) verification of the simulation and experimental results of BS3 on the bottom surface, (b) temperature error.

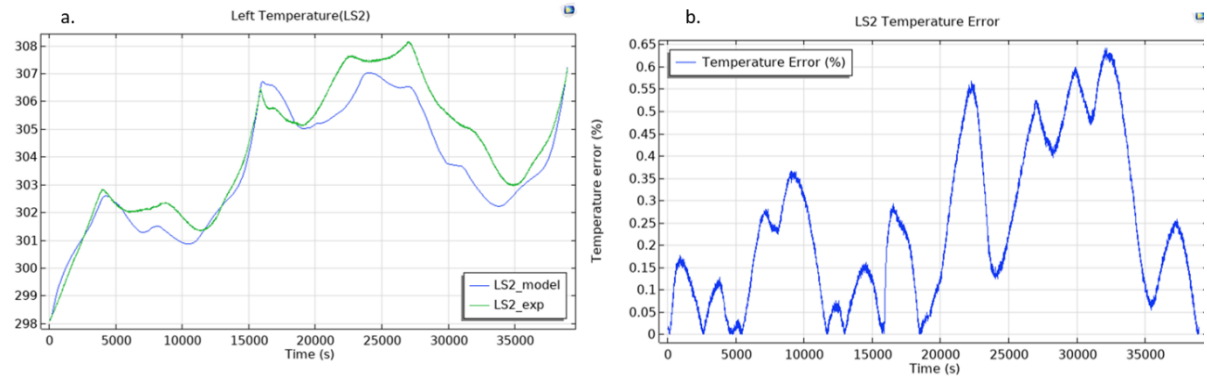

Figure 5.24 Validation of FEM: (a) verification of the simulation and experimental results of LS2 on the left surface, (b) temperature error.

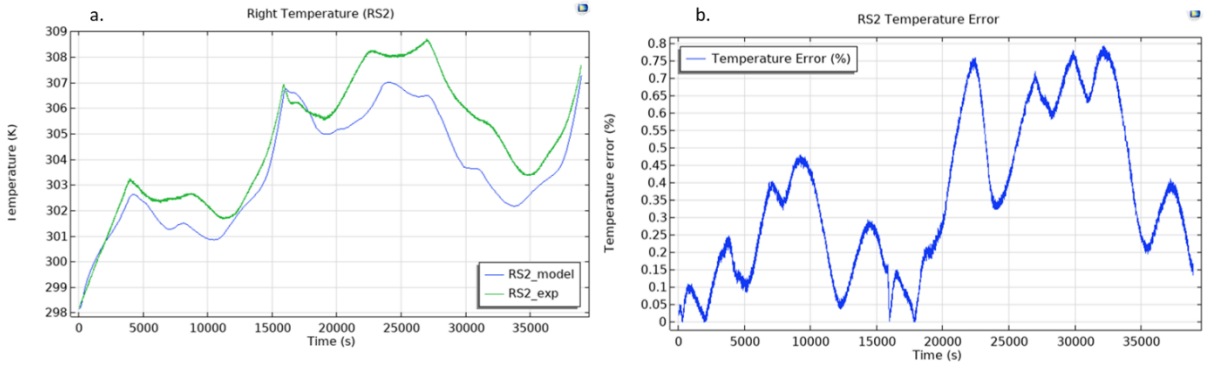

Figure 5.25 Validation of FEM: (a) verification of the simulation and experimental results of RS2 on the right surface, (b) temperature error.

The validation of both the surface average temperature and individual point temperatures of the cell underscored the low level of temperature error. This

outcome corroborates the exceptional performance of the FEA heat transfer model, which is able to delivers accurate and reliable temperature distribution results.

5.3. Performance analysis

To delve into the analysis of the simulation results obtained from the electro-thermal 3D model, the discussion will be structured around two main aspects in the following section: the source of heat generation and the distribution of temperature within the cell structure.

5.3.1. Heat source and thermal behaviors analysis

The simulations adeptly captured the overarching thermal behavior of the cell. **Figure 5.26** illustrated the comprehensive heat generation during the load cycle. Entropic heat varies between positive and negative values. Joule heat, on the other hand, is consistently positive and directly correlates with the SOC level, or more precisely, the current. Focusing on Joule heating (**Figure 5.27**), a significant portion of the heat was contributed by the heat generated from R2. The generated heat from R0 and R1 maintained a consistent trend, whereas the heat generation from R2 exhibits an opposing trend. Additionally, it's noteworthy that the switch point for current direction corresponds to the turning point for joule heat generation.

Concentrating on the discharge and charge phases occurring between 1.2 hours and 7.5 hours, both the discharge and charge phases can be divided into two distinct stages, seen in **Figure 5.28**. In the discharge scenario, the initial stage corresponded to a gradual temperature decline from approximately 100% to 40% SOC within approximately 1.7 hours. This phenomenon stems from the fact that the entropic heat is negative, implying an endothermic process, occasionally even the entropy effects nearing zero in this range. Subsequently, the discharge entered a second stage from 40% to 0% SOC, showing a pronounced temperature increase. The elevation in temperature is attributed to the combined contributions of joule heat and entropic heat. Conversely, during the following full charge phase, the initial stage involved a temperature decrease from 0% to 30% due to the negative entropic heat. As the charging process ensued, coupled with

an increase in current, the heat generated by the Joule effect intensified. This, in turn, resulted in a temperature rise in the subsequent stage, ultimately reaching 100% SOC. Tardy also conducted research on similar topics and discovered that the thermal behavior of the cell was relatively consistent during the charging phase [80]. However, discrepancies arise during the discharge phase. This difference might be attributed to variations in the C rate of the applied current between his study and this model. The different C rate may result in varying effects of entropy on the total heat generation.

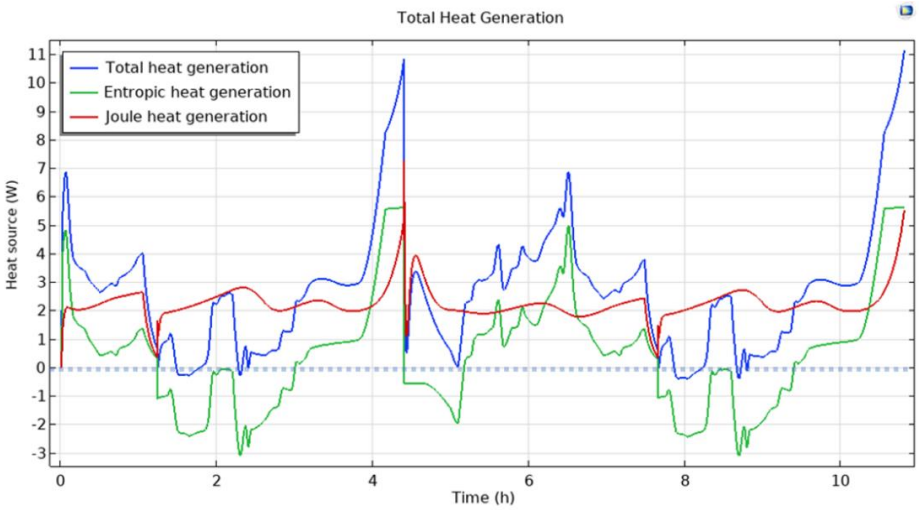

Figure 5.26 Heat source of the total heat generation.

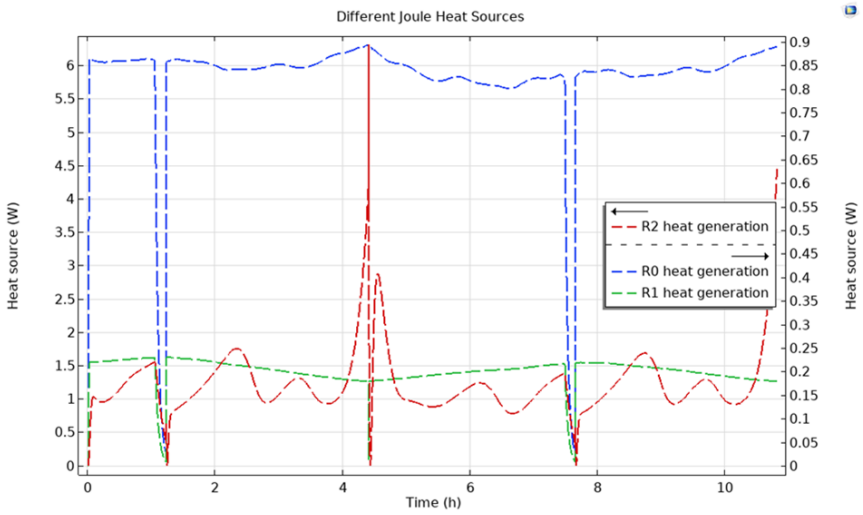

Figure 5.27 Different joule heat sources.

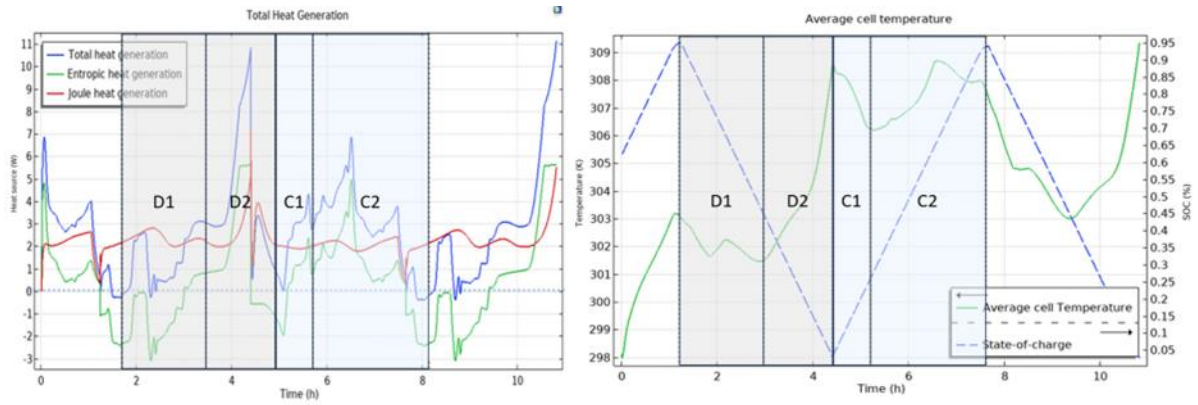

Figure 5.28 Two stages of discharge and charge.

5.3.2. Temperature distribution

Figure 5.29 to **Figure 5.35** exhibited the internal temperature distributions of the cell at various SOC levels. With a 1-second time interval for computations, the obtained results showed a notably homogeneous temperature distribution within the cell's geometry. The maximum temperature difference (ΔT) observed throughout the load cycle across the entirety of the cell's structure was approximately 2K. In regions enveloped by tapes, such as areas on the current collectors, the temperature registered slightly higher than other components. Besides, the central regions of the cell's front and back surfaces, coinciding with the central part of the jelly roll, exhibited higher temperatures due to their high in-plane thermal conductivity.

Regarding the temperature fluctuations within the cell's internal structure throughout the load cycle, the results revealed that the temperature of each component increased from 298K to approximately 303K during the charging process, from the initial SOC of 62.5% to 100% SOC. As previously discussed in the preceding section, the cell's temperature declined due to the endothermic entropy effect during discharge until reaching 40% SOC (**Figure 5.31**). Upon discharging to 0% SOC, the temperature continued to rise, reaching an average temperature of 307K (**Figure 5.32**). Upon initiating the charging phase, the cell's temperature decreased by 2K until it reached 30% SOC (**Figure 5.33**). Upon reaching full charge, the cell's temperature increased to 307K (**Figure 5.34**).

The simulated temperature distribution and changing patterns offer valuable insights into devising an appropriate cooling strategy for this cell. Given the with higher temperature, including the taped sections and the central part of the large surfaces, throughout the load cycle, it is advisable to incorporate cold plates within the clamping. These cold plates would enclose the cell's front and back surfaces, facilitating effective cooling. Considering that cells are typically used to form pack in vehicles, an additional cold plate could be integrated at the bottom to cool the entire pack, which would yield even more efficient cooling effects. Furthermore, it's observed that the cell's temperature tends to increase at both extreme low and high SOC levels, as well as after prolonged cycling. Aiming this, the Battery Thermal Management System (BTMS) should be employed to actively monitor the cell's SOC, particularly after extended operational periods, in order to prevent the temperature from rising to uncontrollable levels.

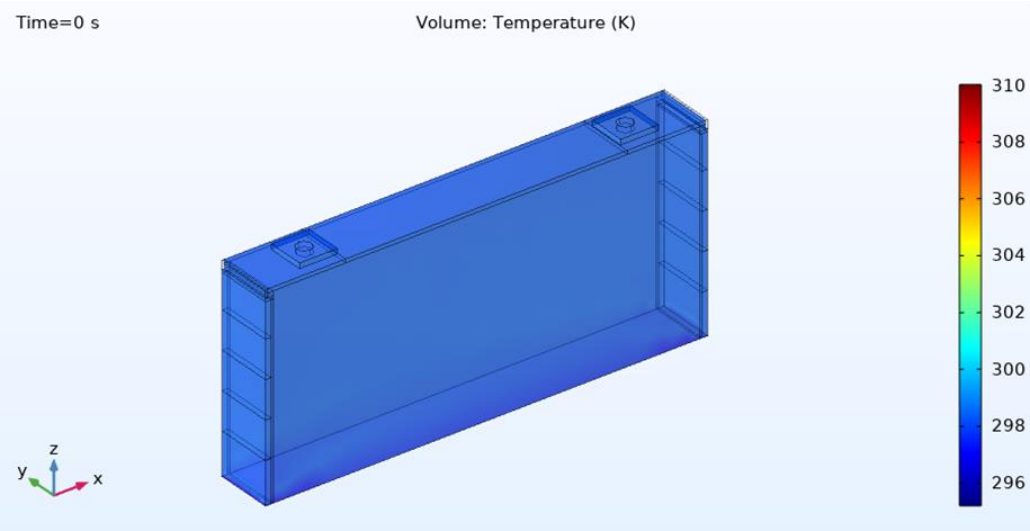

Figure 5.29 Temperature distribution of the cell at the start point.

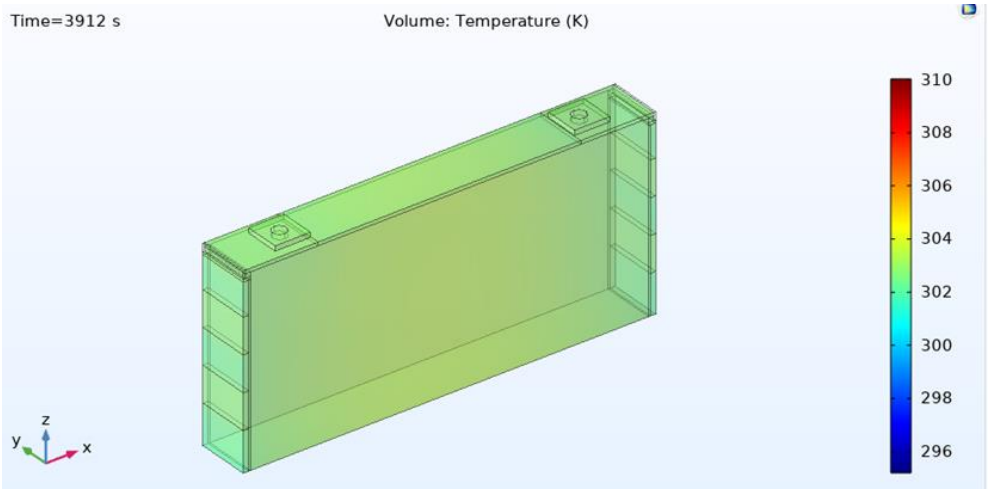

Figure 5.30 Temperature distribution of the cell at 3912 s (100% SOC).

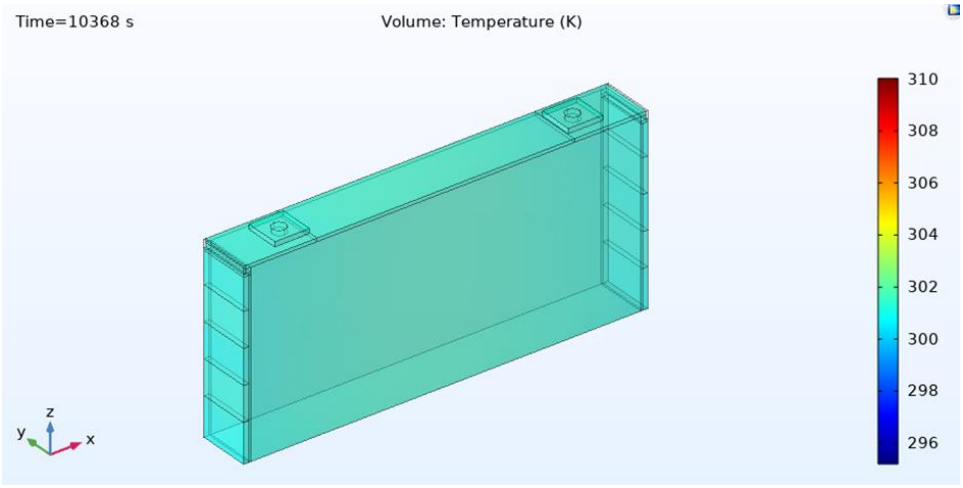

Figure 5.31 Temperature distribution of the cell at 10368 s (40% SOC at discharge).

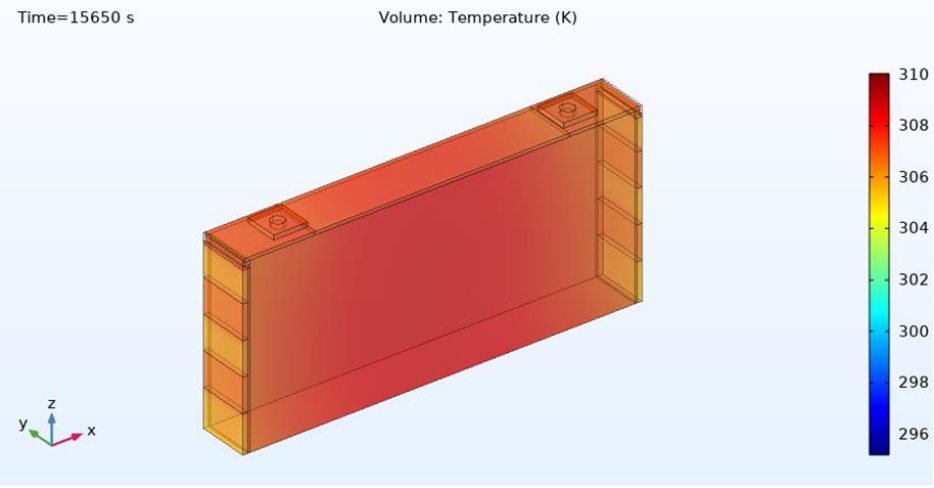

Figure 5.32 Temperature distribution of the cell at 15650 s (0% SOC).

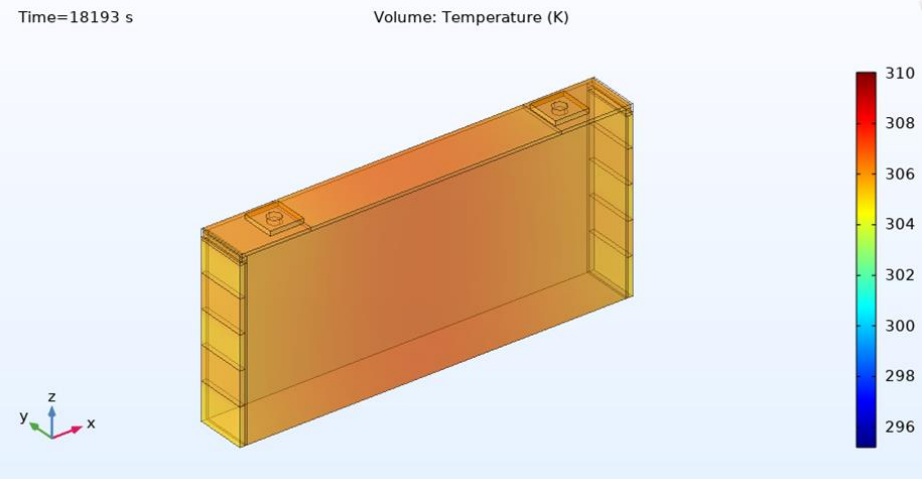

Figure 5.33 Temperature distribution of the cell at 18193 s (30% SOC at charge).

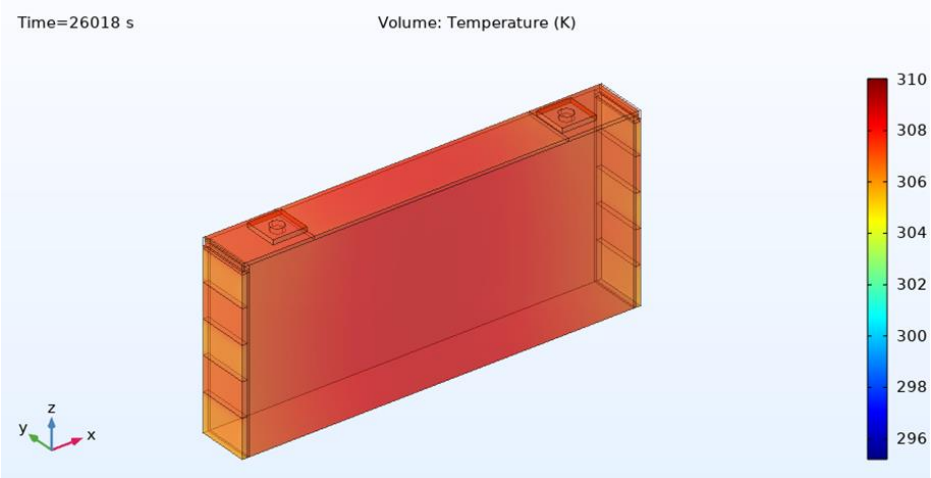

Figure 5.34 Temperature distribution of the cell at 26018 s (100% SOC).

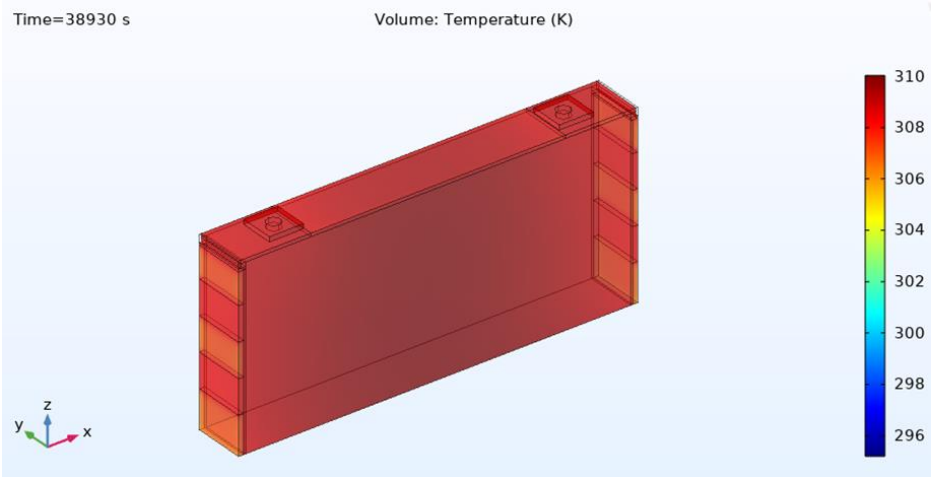

Figure 5.35 Temperature distribution of the cell in the end

6. Summary and conclusions

6.1. Conclusion

Operational temperature significantly impacts the performance of LiB cells. Both high and low temperatures can affect cell's performance and overall functionality. Hence, implementing effective battery thermal management is crucial.

In order to propose a detailed thermal management strategy tailored to this cell with nickel-rich cathodes and enhance its performance in an automotive environment, this thesis has established an electro-thermal 3D model through COMSOL, which integrated the 2RC-ECM for heat generation with the FEA heat transfer model based on the cell's geometry. The simulation results showed the load cycles and internal temperature distributions during cell operation. These results contribute to understanding the electrical and thermal behavior of the cell under different cycling conditions and support the optimization of cooling strategies for the cell. Based on this, some important conclusions could be summarized.

- The developed model has undergone rounds of validation: the ECM has been validated through various current conditions, yielding an average voltage error of 2%. Similarly, the FEA heat transfer model's validation involved average surface and point temperatures, with temperature errors below 1%. These results underscore the model's exceptional performance and reliability.
- During cell cycling, the entropy primarily influences the cell's temperature at low C-rate, while at high C-rate, temperature is primarily governed by the Joule effect. With a current of 1/3C, the entropy change could even effectively serve as a cooling contributor and the primary source of joule heat generation was attributed to R2.
- Regarding the internal temperature distribution of the cell, a homogeneous temperature distribution was observed within the cell's geometry, with a maximum temperature difference (ΔT) of 2K.

- The regions near current collectors and the central part of the cell's front and back surfaces exhibited higher temperatures during cycling, which could provide valuable insights for optimizing cooling strategies for the cell.

6.2. Future work

The satisfactory simulation results obtained in this thesis demonstrate some insights for the optimization of cell’s cooling strategies. Considering the thermal behaviors and high temperature area of the cell observed through simulation results, it is recommended to integrate cold plates enclosing the cell's front and back surfaces like clamping. If time permits, it is expected to develop the model for the cold plates and evaluate the cooling effectiveness, which would serve as a preliminary step for the testing setup for cooling methods. Additionally, there is an interest in exploring the thermal behaviors connecting the cell to the module and pack, with a focus on understanding the correlations and distinctions among for improving simulation models and testing environments.

7. References

[1] Global EV Outlook 2020 – Analysis - IEA, (n.d.). https://www.iea.org/reports/global-ev-outlook-2020 (accessed March 14, 2023).

[2] Progress in batteries and solar cells. 1990, (1990). https://www.osti.gov/biblio/5558986 (accessed March 14, 2023).

[3] A. Pesaran, S. Santhanagopalan, G.H. Kim, Addressing the impact of temperature extremes on large format li-ion batteries for vehicle applications (presentation), National Renewable Energy Lab.(NREL), Golden, CO (United States), 2013.

[4] Z. Chen, D.L. Danilov, Q. Zhang, M. Jiang, J. Zhou, R.-A. Eichel, P.H.L. Notten, Modeling NCA/C6-Si battery ageing, Electrochimica Acta. 430 (2022) 141077. https://doi.org/10.1016/j.electacta.2022.141077.

[5] H. Liu, Z. Wei, W. He, J. Zhao, Thermal issues about Li-ion batteries and recent progress in battery thermal management systems: A review, Energy Conversion and Management. 150 (2017) 304–330. https://doi.org/10.1016/j.enconman.2017.08.016.

[6] P.U. Nzereogu, A.D. Omah, F.I. Ezema, E.I. Iwuoha, A.C. Nwanya, Anode materials for lithium-ion batteries: A review, Applied Surface Science Advances. 9 (2022) 100233. https://doi.org/10.1016/j.apsadv.2022.100233.

[7] E. Wikner, Ageing in Commercial Li-ion Batteries: Lifetime Testing and Modelling for Electrified Vehicle Applications, Chalmers University of Technology, 2019. https://research.chalmers.se/en/publication/512004 (accessed March 27, 2023).

[8] Ethical Supply: The Search for Cobalt Beyond the Congo, Visual Capitalist. (2020). https://www.visualcapitalist.com/sp/ethical-supply-the-search-for-cobalt-beyond-the-congo/ (accessed August 23, 2023).

[9] E. Kamali-Heidari, A. Kamyabi-Gol, M. Heydarzadeh sohi, A. Ataie, Electrode Materials for Lithium Ion Batteries: A Review, JUFGNSM. 51 (2018). https://doi.org/10.22059/jufgnsm.2018.01.01.

[10] G.G. Amatucci, J.M. Tarascon, L.C. Klein, CoO2, The End Member of the Li x CoO2 Solid Solution, J. Electrochem. Soc. 143 (1996) 1114–1123. https://doi.org/10.1149/1.1836594.

[11] A. Jrondi, G. Nikiforidis, M. Anouti, Anion effect on Li/Na/K hybrid electrolytes for Graphite//NCA (LiNi0.8Co0.15Al0.05O2) Li-ion batteries, Journal of Energy Chemistry. 64 (2022) 451–462. https://doi.org/10.1016/j.jechem.2021.05.004.

[12] J. Chidiac, L. Timperman, M. Anouti, Salt and Solvent effect on physicochemical properties and species organisation of Lithium fluorosulfonyl imide (FSI and TFSI) based electrolytes for Li-ion battery: Consequence on cyclability of LiNi0.8Co0.15Al0.05 (NCA) cathode, Journal of the Taiwan Institute of Chemical Engineers. 126 (2021) 88–101. https://doi.org/10.1016/j.jtice.2021.06.049.

[13] V.L. Martins, Advances on liquid electrolytes for Li-ion and Li metal batteries, Current Opinion in Electrochemistry. 38 (2023) 101241. https://doi.org/10.1016/j.coelec.2023.101241.

[14] The Complex Nature of the Electrode/Electrolyte Interfaces in Li-ion Batteries : Towards Understanding the Role of Electrolytes and Additives Using Photoelectron Spectroscopy, (n.d.). https://www.diva-portal.org/smash/record.jsf?pid=diva2%3A699240&dswid=-8340 (accessed March 29, 2023).

[15] L. Sheng, X. Xie, C. Arbizzani, L. Bargnesi, Y. Bai, G. Liu, H. Dong, T. Wang, J. He, A tailored ceramic composite separator with electron-rich groups for high-performance lithium metal anode, Journal of Membrane Science. 657 (2022) 120644. https://doi.org/10.1016/j.memsci.2022.120644.

[16] S. Luiso, P. Fedkiw, Lithium-ion battery separators: Recent developments and state of art, Current Opinion in Electrochemistry. 20 (2020) 99–107. https://doi.org/10.1016/j.coelec.2020.05.011.

[17] T. Maltsev, Thermal behaviour of Li-ion cell : Master Thesis project at Volvo GTT ATR, 2012. https://urn.kb.se/resolve?urn=urn:nbn:se:kth:diva-142488 (accessed May 23, 2023).

[18] Model S | Tesla, (n.d.). https://www.tesla.com/models (accessed March 9, 2023).

[19] J.W. Choi, D. Aurbach, Promise and reality of post-lithium-ion batteries with high energy densities, Nature Reviews Materials. 1 (2016) 16013. https://doi.org/10.1038/natrevmats.2016.13.

[20] A.K. Vatsavai, Electro-thermal modeling of a battery cell set-up, (2020). https://hdl.handle.net/20.500.12380/303946 (accessed May 23, 2023).

[21] Pics/Info: Inside the battery pack | Tesla Motors Club, (n.d.). https://teslamotorsclub.com/tmc/threads/pics-info-inside-the-battery-pack.34934/ (accessed May 30, 2023).

[22] J. Shim, Electrochemical analysis for cycle performance and capacity fading of a lithium-ion battery cycled at elevated temperature, Journal of Power Sources. 112 (2002) 222–230. https://doi.org/10.1016/S0378-7753(02)00363-4.

[23] K.-J. Park, M.-J. Choi, F. Maglia, S.-J. Kim, K.-H. Kim, C.S. Yoon, Y.-K. Sun, High-Capacity Concentration Gradient Li[Ni $_{0.865}$ Co $_{0.120}$ Al $_{0.015}$]O $_{2}$ Cathode for Lithium-Ion Batteries, Adv. Energy Mater. 8 (2018) 1703612. https://doi.org/10.1002/aenm.201703612.

[24] S. Watanabe, M. Kinoshita, T. Hosokawa, K. Morigaki, K. Nakura, Capacity fade of LiAlyNi1−x−yCoxO2 cathode for lithium-ion batteries during accelerated calendar and cycle life tests (surface analysis of LiAlyNi1−x−yCoxO2 cathode after cycle tests in restricted depth of discharge ranges), Journal of Power Sources. 258 (2014) 210–217. https://doi.org/10.1016/j.jpowsour.2014.02.018.

[25] D.P. Abraham, E.P. Roth, R. Kostecki, K. McCarthy, S. MacLaren, D.H. Doughty, Diagnostic examination of thermally abused high-power lithium-ion cells, Journal of Power Sources. 161 (2006) 648–657. https://doi.org/10.1016/j.jpowsour.2006.04.088.

[26] A. Purwanto, C.S. Yudha, U. Ubaidillah, H. Widiyandari, T. Ogi, H. Haerudin, NCA cathode material: synthesis methods and performance enhancement efforts, Mater. Res. Express. 5 (2018) 122001. https://doi.org/10.1088/2053-1591/aae167.

[27] B.-C. Park, H.-B. Kim, H.J. Bang, J. Prakash, Y.-K. Sun, Improvement of Electrochemical Performance of Li[Ni $_{0.8}$ Co $_{0.15}$ Al $_{0.05}$]O $_{2}$ Cathode Materials by AlF $_{3}$ coating at Various Temperatures, Ind. Eng. Chem. Res. 47 (2008) 3876–3882. https://doi.org/10.1021/ie0715308.

[28] F. Leng, C.M. Tan, M. Pecht, Effect of Temperature on the Aging rate of Li Ion Battery Operating above Room Temperature, Sci Rep. 5 (2015) 12967. https://doi.org/10.1038/srep12967.

[29] K. Shah, D. Chalise, A. Jain, Experimental and theoretical analysis of a method to predict thermal runaway in Li-ion cells, Journal of Power Sources. 330 (2016) 167–174. https://doi.org/10.1016/j.jpowsour.2016.08.133.

[30] Q. Wang, P. Ping, X. Zhao, G. Chu, J. Sun, C. Chen, Thermal runaway caused fire and explosion of lithium ion battery, Journal of Power Sources. 208 (2012) 210–224. https://doi.org/10.1016/j.jpowsour.2012.02.038.

[31] X. Feng, M. Fang, X. He, M. Ouyang, L. Lu, H. Wang, M. Zhang, Thermal runaway features of large format prismatic lithium ion battery using extended volume accelerating rate calorimetry, Journal of Power Sources. 255 (2014) 294–301. https://doi.org/10.1016/j.jpowsour.2014.01.005.

[32] B.K. Mandal, A.K. Padhi, Z. Shi, S. Chakraborty, R. Filler, New low temperature electrolytes with thermal runaway inhibition for lithium-ion rechargeable batteries, Journal of Power Sources. 162 (2006) 690–695. https://doi.org/10.1016/j.jpowsour.2006.06.053.

[33] N. Zhang, T. Deng, S. Zhang, C. Wang, L. Chen, C. Wang, X. Fan, Critical Review on Low - Temperature Li - Ion/Metal Batteries, Advanced Materials. 34 (2022) 2107899. https://doi.org/10.1002/adma.202107899.

[34] S.S. Zhang, A review on electrolyte additives for lithium-ion batteries, Journal of Power Sources. 162 (2006) 1379–1394. https://doi.org/10.1016/j.jpowsour.2006.07.074.

[35] N. Xu, J. Shi, G. Liu, X. Yang, J. Zheng, Z. Zhang, Y. Yang, Research progress of fluorine-containing electrolyte additives for lithium ion batteries, Journal of Power Sources Advances. 7 (2021) 100043. https://doi.org/10.1016/j.powera.2020.100043.

[36] S.S. Zhang, K. Xu, T.R. Jow, The low temperature performance of Li-ion batteries, Journal of Power Sources. 115 (2003) 137–140. https://doi.org/10.1016/S0378-7753(02)00618-3.

[37] Q. Li, D. Lu, J. Zheng, S. Jiao, L. Luo, C.-M. Wang, K. Xu, J.-G. Zhang, W. Xu, Li+-desolvation dictating lithium-ion battery's low-temperature performances, ACS Applied Materials & Interfaces. 9 (2017) 42761–42768.

[38] C. Vidal, O. Gross, R. Gu, P. Kollmeyer, A. Emadi, xEV Li-Ion Battery Low-Temperature Effects—Review, IEEE Trans. Veh. Technol. 68 (2019) 4560–4572. https://doi.org/10.1109/TVT.2019.2906487.

[39] M.C. Smart, B.V. Ratnakumar, Effects of Electrolyte Composition on Lithium Plating in Lithium-Ion Cells, J. Electrochem. Soc. 158 (2011) A379–A389. https://doi.org/10.1149/1.3544439.

[40] S. Ma, M. Jiang, P. Tao, C. Song, J. Wu, J. Wang, T. Deng, W. Shang, Temperature effect and thermal impact in lithium-ion batteries: A review, Progress in Natural Science: Materials International. 28 (2018) 653–666. https://doi.org/10.1016/j.pnsc.2018.11.002.

[41] Y. Wang, X. Zhang, Z. Chen, Low temperature preheating techniques for Lithium-ion batteries: Recent advances and future challenges, Applied Energy. 313 (2022) 118832. https://doi.org/10.1016/j.apenergy.2022.118832.

[42] B. Xu, F. Xia, Y. Wang, X. Xie, W. Gan, A battery thermal management scheme suited for cold regions based on PCM and aerogel: Demonstration of performance and availability, Applied Thermal Engineering. 227 (2023) 120378. https://doi.org/10.1016/j.applthermaleng.2023.120378.

[43] D. Ouyang, Y. He, J. Weng, J. Liu, M. Chen, J. Wang, Influence of low temperature conditions on lithium-ion batteries and the application of an insulation material, RSC Adv. 9 (2019) 9053–9066. https://doi.org/10.1039/C9RA00490D.

[44] R. Bisschop, O. Willstrand, F. Amon, M. Rosenggren, Fire Safety of Lithium-Ion Batteries in Road Vehicles, RISE - Research Institutes of Sweden (2017-2019), Safety, 2019.

[45] P. Nelson, D. Dees, K. Amine, G. Henriksen, Modeling thermal management of lithium-ion PNGV batteries, Journal of Power Sources. 110 (2002) 349–356.

[46] G. Xia, L. Cao, G. Bi, A review on battery thermal management in electric vehicle application, Journal of Power Sources. 367 (2017) 90–105. https://doi.org/10.1016/j.jpowsour.2017.09.046.

[47] T. Wang, K.J. Tseng, J. Zhao, Z. Wei, Thermal investigation of lithium-ion battery module with different cell arrangement structures and forced air-cooling strategies, Applied Energy. 134 (2014) 229–238. https://doi.org/10.1016/j.apenergy.2014.08.013.

[48] P. Kumar, D. Chaudhary, P. Varshney, U. Varshney, S.M. Yahya, Y. Rafat, Critical review on battery thermal management and role of nanomaterial in heat transfer enhancement for electrical vehicle application, Journal of Energy Storage. 32 (2020) 102003. https://doi.org/10.1016/j.est.2020.102003.

[49] J. Zhao, Z. Rao, Y. Huo, X. Liu, Y. Li, Thermal management of cylindrical power battery module for extending the life of new energy electric vehicles, Applied Thermal Engineering. 85 (2015) 33–43. https://doi.org/10.1016/j.applthermaleng.2015.04.012.

[50] H. Zhou, F. Zhou, L. Xu, J. Kong, QingxinYang, Thermal performance of cylindrical Lithium-ion battery thermal management system based on air distribution pipe, International Journal of Heat and Mass Transfer. 131 (2019) 984–998. https://doi.org/10.1016/j.ijheatmasstransfer.2018.11.116.

[51] Y. Fan, Y. Bao, C. Ling, Y. Chu, X. Tan, S. Yang, Experimental study on the thermal management performance of air cooling for high energy density cylindrical lithium-ion batteries, Applied Thermal Engineering. 155 (2019) 96–109. https://doi.org/10.1016/j.applthermaleng.2019.03.157.

[52] S. Roger, Packaging of New Servers, Energy Efficiency Aspects: 1st Berkeley Symposium on Energy Efficient Electronics, (2009).

[53] R.W. van Gils, D. Danilov, P.H.L. Notten, M.F.M. Speetjens, H. Nijmeijer, Battery thermal management by boiling heat-transfer, Energy Conversion and Management. 79 (2014) 9–17. https://doi.org/10.1016/j.enconman.2013.12.006.

[54] D. Chen, J. Jiang, G.-H. Kim, C. Yang, A. Pesaran, Comparison of different cooling methods for lithium ion battery cells, Applied Thermal Engineering. 94 (2016) 846–854. https://doi.org/10.1016/j.applthermaleng.2015.10.015.

[55] D.T. Adams, G. Berdichevsky, T.E. Colson, A. Hebert, S. Kohn, D. Lyons, N.J. Mendez, J.B. Straubel, D. West, A. Simpson, Battery pack thermal management system, Google Patents, 2009.

[56] A. Jarrett, I.Y. Kim, Influence of operating conditions on the optimum design of electric vehicle battery cooling plates, Journal of Power Sources. 245 (2014) 644–655. https://doi.org/10.1016/j.jpowsour.2013.06.114.

[57] L.W. Jin, P.S. Lee, X.X. Kong, Y. Fan, S.K. Chou, Ultra-thin minichannel LCP for EV battery thermal management, Applied Energy. 113 (2014) 1786–1794. https://doi.org/10.1016/j.apenergy.2013.07.013.

[58] Y. Huo, Z. Rao, X. Liu, J. Zhao, Investigation of power battery thermal management by using mini-channel cold plate, Energy Conversion and Management. 89 (2015) 387–395. https://doi.org/10.1016/j.enconman.2014.10.015.

[59] J. E, D. Han, A. Qiu, H. Zhu, Y. Deng, J. Chen, X. Zhao, W. Zuo, H. Wang, J. Chen, Q. Peng, Orthogonal experimental design of liquid-cooling structure on the cooling effect of a liquid-cooled battery thermal management system, Applied Thermal Engineering. 132 (2018) 508–520. https://doi.org/10.1016/j.applthermaleng.2017.12.115.

[60] Y. Huo, Z. Rao, The numerical investigation of nanofluid based cylinder battery thermal management using lattice Boltzmann method, International Journal of Heat and Mass Transfer. 91 (2015) 374–384. https://doi.org/10.1016/j.ijheatmasstransfer.2015.07.128.

[61] X.-H. Yang, S.-C. Tan, J. Liu, Thermal management of Li-ion battery with liquid metal, Energy Conversion and Management. 117 (2016) 577–585. https://doi.org/10.1016/j.enconman.2016.03.054.

[62] Y. Pan, Y. Hua, S. Zhou, R. He, Y. Zhang, S. Yang, X. Liu, Y. Lian, X. Yan, B. Wu, A computational multi-node electro-thermal model for large prismatic lithium-ion batteries, Journal of Power Sources. 459 (2020) 228070. https://doi.org/10.1016/j.jpowsour.2020.228070.

[63] S. Arora, W. Shen, A. Kapoor, Neural network based computational model for estimation of heat generation in LiFePO4 pouch cells of different nominal capacities, Computers & Chemical Engineering. 101 (2017) 81–94. https://doi.org/10.1016/j.compchemeng.2017.02.044.

[64] W. Allafi, C. Zhang, K. Uddin, D. Worwood, T.Q. Dinh, P.A. Ormeno, K. Li, J. Marco, A lumped thermal model of lithium-ion battery cells considering radiative heat transfer, Applied Thermal Engineering. 143 (2018) 472–481. https://doi.org/10.1016/j.applthermaleng.2018.07.105.

[65] T.F. Fuller, M. Doyle, J. Newman, Simulation and Optimization of the Dual Lithium Ion Insertion Cell, Journal of The Electrochemical Society. 141 (1994) 1. https://doi.org/10.1149/1.2054684.

[66] R. Xiong, J. Cao, Q. Yu, H. He, F. Sun, Critical Review on the Battery State of Charge Estimation Methods for Electric Vehicles, IEEE Access. 6 (2018) 1832–1843. https://doi.org/10.1109/ACCESS.2017.2780258.

[67] M. Hossain, S. Saha, M.E. Haque, M.T. Arif, A. Oo, A Parameter Extraction Method for the Thevenin Equivalent Circuit Model of Li-ion Batteries, in: 2019 IEEE Industry Applications Society Annual Meeting, 2019: pp. 1–7. https://doi.org/10.1109/IAS.2019.8912326.

[68] D. Karimi, H. Behi, J. Van Mierlo, M. Berecibar, Equivalent Circuit Model for High-Power Lithium-Ion Batteries under High Current Rates, Wide Temperature Range, and Various State of Charges, Batteries. 9 (2023). https://doi.org/10.3390/batteries9020101.

[69] S. Thanagasundram, R. Arunachala, K. Löffler, T. Teutsch, A. Jossen, A Cell Level Model for Battery Simulation, in: 2012.

[70] C. Emvin, J. Persson, W. Åkvist, Virtual Platform for Reinforcement Learning Research for Heavy Vehicles, (2020). https://hdl.handle.net/20.500.12380/300827 (accessed July 4, 2023).

[71] Y. Bai, L. Li, Y. Li, G. Chen, H. Zhao, Z. Wang, C. Wu, H. Ma, X. Wang, H. Cui, J. Zhou, Reversible and irreversible heat generation of NCA/Si–C pouch cell during electrochemical energy-storage process, Journal of Energy Chemistry. 29 (2019) 95–102. https://doi.org/10.1016/j.jechem.2018.02.016.

[72] Q.-K. Wang, Y.-J. He, J.-N. Shen, Z.-F. Ma, G.-B. Zhong, A unified modeling framework for lithium-ion batteries: An artificial neural network based thermal coupled equivalent circuit model approach, Energy. 138 (2017) 118–132. https://doi.org/10.1016/j.energy.2017.07.035.

[73] COMSOL 5.4, Heat Transfer Module Users Guide.pdf, (n.d.). https://doc.comsol.com/5.4/doc/com.comsol.help.heat/HeatTransferModuleUsersGuide.pdf (accessed August 28, 2023).

[74] A.M. Ahmad, G. Thenaisie, S.-G. Lee, A calorimetric approach to fast entropy-variations extraction for lithium-ion batteries using optimized galvanostatic intermittent titration technique, Journal of Power Sources Advances. 16 (2022) 100097. https://doi.org/10.1016/j.powera.2022.100097.

[75] N. Damay, C. Forgez, M.-P. Bichat, G. Friedrich, A method for the fast estimation of a battery entropy-variation high-resolution curve – Application on a commercial LiFePO4/graphite cell, Journal of Power Sources. 332 (2016) 149–153. https://doi.org/10.1016/j.jpowsour.2016.09.083.

[76] Z. Geng, J. Groot, T. Thiringer, A Time- and Cost-Effective Method for Entropic Coefficient Determination of a Large Commercial Battery Cell, IEEE Transactions on Transportation Electrification. 6 (2020) 257–266. https://doi.org/10.1109/TTE.2020.2971454.

[77] J.P. Schmidt, A. Weber, E. Ivers-Tiffée, A novel and precise measuring method for the entropy of lithium-ion cells: ΔS via electrothermal impedance spectroscopy, Electrochimica Acta. 137 (2014) 311–319. https://doi.org/10.1016/j.electacta.2014.05.153.

[78] X.-F. Zhang, Y. Zhao, Y. Patel, T. Zhang, W.-M. Liu, M. Chen, G.J. Offer, Y. Yan, Potentiometric measurement of entropy change for lithium batteries, Phys. Chem. Chem. Phys. 19 (2017) 9833–9842. https://doi.org/10.1039/C6CP08505A.

[79] F. Yun, W. Jin, L. Tang, W. Li, J. Pang, S. Lu, Analysis of Capacity Fade from Entropic Heat Coefficient of Li[NixCoyMnz]O2/Graphite Lithium Ion Battery, J. Electrochem. Soc. 163 (2016) A639. https://doi.org/10.1149/2.0311605jes.

[80] E. Tardy, P.-X. Thivel, F. Druart, P. Kuntz, D. Devaux, Y. Bultel, Internal temperature distribution in lithium-ion battery cell and module based on a 3D electrothermal model: An investigation of real geometry, entropy change and thermal process, Journal of Energy Storage. 64 (2023) 107090. https://doi.org/10.1016/j.est.2023.107090.

8. Appendix

8.1. Temperature distribution test

Step	Type	Mode	Value	Limit	Value	End Type	Op	Value	Goto	Report Type	Value	Options
1	Rest					Step Time	=	00:00:05	002	Step Time	00:00:01	ANNN
						Voltage	>=	4,3	011			
						Voltage	<=	2,7	011			
						Thermocouple	>=	1 / 50,0	011			
						Thermocouple	>=	2 / 50,0	011			
						Thermocouple	>=	3 / 50,0	011			
2	Rest					Step Time	=	00:01:00	003	Step Time	00:01:00	ANNN
										Voltage	1,0	
3	Rest					Thermocouple	<=	3 / 26,0	004	Step Time	00:01:00	ANNN
										Voltage	1,0	
										Thermocouple	1 / 1,0	
4	Discharge	Current	0,3C			Step Time	=	02:00:00	005	Step Time	00:00:01	ANNN
						Voltage	<=	2,8	005	Voltage	0,01	
						Thermocouple	<=	1 / 45,0	005	Current	0,1	
5	Rest					Thermocouple	<=	1 / 26,0	006			ANNN
6	Do1											
7	Charge	Current	0,3C	Voltage	4,2	Step Time	=	04:00:00	008	Step Time	00:00:01	ANNN
						Current	<=	0,05C	008	Voltage	0,01	
						Thermocouple	>=	1 / 45,0	008	Current	1,0	
8	Discharge	Current	0,3C			Step Time	=	04:00:00	009	Step Time	00:00:01	ANNN
						Thermocouple	>=	1 / 45,0	009	Voltage	0,01	
						Voltage	<=	2,8	009	Current	1,0	
9	Loop1					Loop Count	=	10	010			
10	Rest					Step Time	=	01:00:00	011	Step Time	00:01:00	ANNN
										Voltage	1,0	
												ANNN
11	Rest					Thermocouple	<=	3 / 26,0	012	Step Time	00:01:00	
										Voltage	1,0	
										Thermocouple	1 / 1,0	
12	End											

Figure 36 Temperature distribution test procedure

8.2. Entropy coefficient measurement

Step	Type	Mode	Value	Limit	Value	End Type	Op	Value	Goto	Report Type	Value	Options
1	Rest					Step Time	=	00:00:10	002	Step Time	00:00:01	ANNN
						Voltage	>=	4.3	016	Set Variable	atEnd: VAR1=150.832	
						Voltage	<=	2.7	016			
						Thermocouple	>=	1 / 50.0	016			ANNN
2	Rest					Thermocouple	>=	1 / 28.0	003			
3	Do1											
4	Rest					Step Time	=	04:00:00	005	Step Time	00:00:10	ANNN
										Voltage	0.01	
5	Rest					Thermocouple	<=	1 / 21.0	006	Voltage	0.01	ANNN
										Step Time	00:00:10	
6	Rest					Step Time	=	04:00:00	007	Step Time	00:00:10	ANNN
										Voltage	0.01	
7	Rest					Thermocouple	<=	1 / 14.0	008	Voltage	0.01	ANNN
										Step Time	00:00:10	
8	Rest					Step Time	=	04:00:00	009	Step Time	00:00:10	ANNN
										Voltage	0.01	
9	Rest					Thermocouple	>=	1 / 28.0	010	Voltage	0.01	ANNN
										Step Time	00:00:10	
10	Discharge	Current	0.33C			Step Time	=	00:40:00	011	Step Time	00:00:01	ANNN
						Thermocouple	>=	1 / 40.0	011	Current	0.1	
						Function	:	CAPACITY>=VAR1*0.1	011	Voltage	0.01	
										Thermocouple	1 / 1.0	
11	Loop1					Loop Count	=	10	012			
											00:00:10	ANNN
12	Rest					Step Time	=	04:00:00	013	Step Time	0.01	
										Voltage		
											00:00:10	ANNN
13	Rest					Step Time	=	04:00:00	014	Step Time	0.01	
										Voltage		
											00:00:10	ANNN
14	Rest					Step Time	=	04:00:00	015	Step Time	0.01	
										Voltage		
											0.01	ANNN
15	Charge	Current	0.5C	Voltage	4.2	Thermocouple	>=	1 / 45.0	016	Voltage	00:00:10	
						Current	<=	0.05C	016	Step Time	0.01	
						Function	:	CAPACITY>=VAR1*0.5	016	Voltage		
						Step Time	=	02:00:00	016			
16	End											

Figure 37 Potentiometric entropy test procedure